Submitted to Ap. J. Suppl.

Catalog of Four-Color Photometry of Stars, Galaxies, and QSOs using SDSS Filters

Heidi Jo Newberg,[1,5] Gordon T. Richards,[1,2] Michael Richmond,[3] Xiaohui Fan[4]

ABSTRACT

We present a catalog containing the measurements of 2262 sources, including 334 extended sources, 1915 point sources, and 13 known QSOs, in five SDSS passbands. Of these objects, over 1600 are measured in 15 fields covering 0.5 square degrees, with a limiting magnitude of $r^* < 19.5$, similar to the photometric limit of the SDSS spectroscopic survey. Color plots of the data show that stars, galaxies, and quasars are fairly well separated by color alone. The stellar locus populates a ribbon-like subset of color-color-color space. It is shown that stars, galaxies, and QSOs tend towards the same fundamental plane in three-dimensional color space. The stars are compared with synthetic photometry from Kurucz models; the agreement is consistent with the errors in the data. The stellar locus moves in color space by about a tenth of a magnitude from $r^* = 14$ to $r^* = 19.5$. The shift is consistent with a shift in the metallicity from about [Me/H] = -1 to [Me/H] = -2. We compare this with previously measured metallicity gradients as a function of distance from the galactic plane.

Subject headings: catalogs, stars: general, stars: fundamental parameters, galaxies: photometry, quasars: general

1. Introduction

The Sloan Digital Sky Survey (SDSS) is projected to produce a photometric catalog for on the order of 100 million astronomical objects early in the 21st century. Spectra will be obtained for one

---

[1] Fermi National Accelerator Laboratory, Kirk Road and Pine Street, Batavia, IL 60510; heidi@fnal.gov

[2] Department of Astronomy and Astrophysics, University of Chicago, 5640 S. Ellis Avenue, Chicago, IL 60637; richards@oddjob.uchicago.edu

[3] Dept. of Physics, Rochester Institute of Technology, Rochester, NY 14623-5603; mwrsps@rit.edu

[4] Princeton University, Peyton Hall, Princeton, NJ 08544; fan@astro.princeton.edu

[5] work supported by the U. S. Department of Energy under contract No. DE-ACO2-76CH03000

million of the brightest galaxies and 100 thousand QSOs from this catalog. This survey achieved first light on the telescope and imaging camera in May, 1998. The data from the imaging portion of the survey will be obtained in five passbands: u', g', r', i', and z'. These passbands were designed specifically for the Sloan survey, and do not yet correspond to a photometric system; the system will be defined as part of the initial operational phase of the survey.

It is important to collect data with these filters in advance of the survey for two reasons. First, it is of utmost importance to the SDSS that the selection criteria for the spectroscopic portion of the survey be well understood in advance, in order to maximize the science from each fiber while keeping the selection criteria constant. The spectroscopic survey cannot begin until the selection criteria for QSOs are well understood. Second, it is important to the science community to understand the properties of celestial objects in this system in order to exploit the data when it becomes available.

For these purposes, we have obtained photometry for over 2000 sources in five passbands. The filters and the CCD are similar to the ones which will be used in the SDSS. The SDSS photometric system, (u', g', r', i', and z'; Fukugita et al. 1996), is similar to the AB_ν system from Oke and Gunn (1983), but is not identical. Since the definition of the SDSS photometric system is still in progress, and there exists no other system to which to tie the observations, we have calibrated our own set of secondary standards from the SDSS primary standard BD +17°4708. Since our system differs from the final SDSS system, we designate the filter system used in our observations as u^*, g^*, r^*, i^*, and z^*, in keeping with the convention of Richards et al. (1997). We include the calibration of our secondary standards so that when the final SDSS system is agreed upon, our photometry can be translated to that system.

2. Observations

We present a catalog of objects detected in 22 fields (Table 1) covering about 0.8 square degrees of sky. All fields were observed in five optical passbands: u^*, g^*, r^*, i^*, and z^*. The majority of the fields (over 0.5 square degrees) have been cataloged to $r^* \sim 19.5$. Thirteen of the fields were chosen to contain a known quasar in the redshift range $2.5 < z < 3.5$. The others were chosen either as standard stars or to calibrate USNO astrometric patches. The standard star fields were exposed only long enough to sample the targeted star, so the photometry for these fields is not as deep.

The observations were obtained with the 1.0 m telescope at the U. S. Naval Observatory in Flagstaff, AZ in three separate dark runs: Nov. 7-11, 1996, Dec. 11-16, 1996 and Jan. 6-10, 1996. The telescope is equipped with filters which are identical to the ones which will define the SDSS u', g', r', i' and z' system. The CCD is a UV-coated SITE 1024 x 1028 CCD which differs from the camera for the SDSS monitor telescope only in its size. With a pixel scale of approximately 0.675”, it has a field-of-view 11.5 arc minutes across.

We used data from the four best nights of observing: Nov. 9 (day 315), Nov. 11 (day 317), Dec. 12 (day 348), and Dec. 13 (day 349). The nights were clear, but not totally photometric, and the seeing varied substantially throughout the night (see Table 2 for measured widths in each image).

3. Data Reduction

The data reductions were performed using software under development for the Sloan Digital Sky Survey. The SDSS common code is built in the DERVISH/ASTROTOOLS environment (Sergey et al. 1996; previously known as the SHIVA environment, but the name was changed to avoid conflict with the SHIVA Corporation), and is easily modified to the specific data processing task. Since we did not use a commonly used astronomical package, we describe the essential steps in the reduction process.

3.1. Image Correction

Bias vectors and flatfields were calculated once per dark run. An inspection of bias frames showed that they varied from column to column, but that the small variations from row to row were not consistent from frame to frame, so the bias frames were compressed to a row vector. An attempt was made to remove the row-to-row variation in the data images by subtracting from a given row the average value in the bias columns from 20 rows before to 20 rows after this row. Flatfields were generated for each filter from at least a dozen (and sometimes two dozen) well-exposed twilight sky images. Sky frames were normalized to one in a central region of the CCD. The mean flatfield was generated, rejecting individual pixels with values more than 3 standard deviations from the mean for that position on the CCD.

We observed significant fringing from airglow emission lines in the i^* and z^* frames. The fringing does not appear in the sky flats, and thus does not affect our flatfield corrections, since the twilight sky is nearly a continuum spectrum. The fringes did not move significantly during the night, and are reasonably well correlated with the sky brightness in a particular image, so we were able to subtract off a fringe frame (scaled in proportion to the image sky value) to remove the fringes. The fringe frame was created by coadding all instances of each deep star field (standard star fields were not used), scaling the coadded frames so that the sky value was one, and then finding the clipped mean (with 5σ clipping) image.

3.2. Object Finding

First a global sky value (and its error) was determined by using a clipped mean (3σ clipping) over the entire image. Objects were then found by looking for pixels with signal greater than

10σ above the global sky value and requiring that such peaks also be local maxima (signal at least as great as the 8 adjacent pixels). Objects within 5 pixels of the edge of the chip were not considered. Objects whose peak pixel value was above the limit for linear (to one percent) response from the CCD were discarded. For each detected peak, a centroid was determined from the intensity-weighted first moments within a 5 pixel radius surrounding the peak.

3.3. Determining the Aperture Size

The optics on the 1.0m telescope at the USNO are such that the measured seeing cannot get much better than $2.0''$, and we found that during the course of a night the seeing varied between just slightly better than $2.0''$ up to over $5.0''$. As a result it was impossible to use a single aperture size for all the frames on a given night, since that aperture would not represent a reasonably constant fraction of the light. Therefore we chose to use a different aperture size (based on the seeing conditions) for each frame. Specifically, the average FWHM of the objects in each frame was used as the aperture radius for that frame. In §3.5 we describe how these measurements were placed on a common scale.

The FWHM of each object was determined from the best fit circularly symmetric Gaussian. Then the aperture for each frame was determined by taking the median FWHM of the 20 brightest unsaturated objects on the frame that had widths consistent with stars. In the r^* filter this resulted in apertures between $2.46''$ and $4.25''$. If stellar profiles were Gaussians, this would give the same fraction of light in every aperture.

3.4. Object Measuring

For purposes of determining the number of counts (and the error in the counts) in an object, each pixel was subdivided into a 10×10 grid, with each subpixel assigned one hundredth of the light in the pixel. A local sky value was determined for each object by using a sigma clipping algorithm with a setting of 3σ for 5 iterations on a sky annulus between 6 and 10 pixels. Then the number of counts was calculated as the sum of the sky-subtracted counts in each subpixel within a radius given by the calculated FWHM for the image. Objects with a FWHM < 1.8 pixels were thrown out as spurious sources. In addition, sources with insignificant integrated counts or with unusual profiles were dropped. Objects for which the FWHM in the r^* frame was more than ten percent larger than the typical FWHM for stars were flagged as galaxies.

As a check on our photometry we also did a preliminary reduction with DAOPHOT in IRAF and found that the count rates determined with our SDSS software agree with the IRAF results to much better than 1 percent. For this test a fixed aperture with 3 pixel ($2.025''$) radius was used in both software packages.

We checked our separation of stars and galaxies using artificial stars. Figure 1a shows the distribution in fractional FWHM variation for catalog objects with $18.5 < r^* < 19.5$, including the cut at 0.1 that was used to separate stars from galaxies. Figure 1b shows the same distribution for simulated stars in one of the images (UM 673). The simulated stars were generated by excising 8 bright, isolated stars in the frame, then scaling down the counts to simulate an $r^* = 19.5$ magnitude object, and then adding each one back in 100 places in the image. The placement of the grid of simulated stars was offset slightly for each of the eight sets so that no two simulated stars were placed in the same spot on the CCD. One of us (H.N.) then looked at each simulated star by hand to reject simulated stars which would have been rejected in the catalog (see §5). Forty-five of the 800 placements were rejected. About 2.4% of the simulated stars had measured widths which would cause them to be classified as galaxies; stars with large widths were often chance placements near another object. If real stars are misclassified with the same frequency, then about 10 of the faint extended sources (5% of the galaxies fainter than $r^* = 18.5$) are really stars.

3.5. Aperture Correction

Since our standard stars were observed with high signal-to-noise, we were able to minimize the systematics by using a large (25 pixel radius) aperture to integrate the light from these stars, and a larger (25 to 30 pixel) annulus to measure the sky. This large aperture contained essentially all of the light from the standard stars - even those which required defocusing to keep them in the linear operating range of the CCD. In order to be able to calibrate our program stars, which were typically measured within an aperture of five or six pixels, we applied an aperture correction. Since the apertures and point spread functions varied substantially from field to field, we calculated a separate correction for each field. The calculation of this correction must be carefully tuned; it requires stellar objects with high signal-to-noise whose photometry is not affected by other sources within seventeen arc seconds.

Individual estimates of the aperture correction were determined for each object by taking the ratio of the sky-subtracted counts from 0 to 25 pixels to the sky-subtracted counts found within the aperture used for the program stars. In order to minimize the impact of other sources within the 25 pixel radius, we did not strictly add up the light within the large aperture. The number of counts within 5 pixels of the centroid was determined as above. Then, for each of five equally-spaced annuli between 5 pixels and 25 pixels, a sky-subtracted, clipped mean (two sigma clipping) was found. The counts in the central region were added to the mean counts in each annulus times the number of pixels in each annulus. The estimate of the aperture correction is the ratio of the sky-subtracted counts in the larger aperture to the sky-subtracted counts found in the smaller aperture.

The aperture correction for each frame was then determined from the aperture correction estimates from the 5 brightest stars satisfying the following criteria: aperture correction greater than 1.0 and less than 2.0, counts in the 5 pixel aperture greater than $10,000$, and FWHM within ten percent of the expected FWHM for that frame. The aperture corrections are tabulated in Table

2.

The count rate for each object in a frame is the number of counts within the aperture with a radius equal the frame FWHM, divided by the exposure time, and multiplied by the aperture correction. The error in the count rate was calculated from photon statistics (including sky background) using a value of 7.43 electrons/ADU for the gain and 6 electrons for the read noise.

3.6. Matching Objects in Different Passbands

After the data from each filter was reduced, objects were matched between filters. The row and column coordinates of a special object (usually a standard star or known quasar) were determined by hand. These coordinates (one set for each filter) were subtracted from the measured centroids of every object on a frame. Magnification, rotation, and shear were not necessary to align the filters. Objects were matched between filters if their positions with respect to the special object were the same to within five pixels.

4. Astrometric and Photometric Calibration

Since our field of view was small, only about $12'$ on a side, we may treat our images as simple projections of the spherical sky onto a planar detector. We identified between 6 and 12 stars in each image which appear in the Hubble Guide Star Catalog (Russell et al. 1990, Lasker et al. 1990) and projected the coordinates of each GSC star onto a plane with tangent point at the center of the image, following Olkin et al. (1996). We then calculated a linear transformation between the (row, col) position of stars in the CCD image and the (ξ, η) coordinates in the tangent plane. We applied the transformation to the coordinates of all objects in the image, then inverted the projection to yield final spherical coordinates (RA, Dec). Residuals between our measured positions of the GSC stars and their catalog values are typically one arc second.

The photometric calibration was tricky, since the SDSS system has not yet been established. We therefore needed not only to find the atmospheric extinction and the zeropoints for the detector, but we also had to define our own photometric system. Since we observed at small airmasses (1.0 to 1.4), we decided to ignore color-dependent extinction terms; their effects were smaller than the typical scatter in our solutions. This simplified the analysis, allowing us to reduce the data in each passband independently (remember, we were not matching our measurements to an existing system, but using our instrument to *define* a magnitude scale; we required no color terms in our solutions).

During each night, we measured a number of stars which will be used as standards for the SDSS system. The star BD +17°4708 will serve as the fundamental standard of the SDSS system; its magnitude in the SDSS system will be 10.56, 9.64, 9.35, 9.25, and 9.23 in u', g', r', i', and z', respectively (Fukugita et al. 1996). We used this star to set the zeropoint of our results, which should resemble closely the official SDSS values. However, if the USNO telescope and camera have a different photometric response than the instrument used to define the SDSS system, our magnitudes may differ from official SDSS magnitudes by a few percent. We therefore label our passbands u^*, g^*, r^*, i^* and z^* to emphasize their provisional nature. In Table 3 we list the measured magnitudes for nine standard stars which are likely to be included in the definition of the SDSS photometric system, so that the photometry in this paper can one day be compared to the true SDSS system.

We now describe in detail the process by which we converted instrumental into calibrated magnitudes. The instrumental magnitudes for each standard star were found in an aperture with a 25 pixel ($16.875''$) radius. This large aperture was necessary since in many cases the bright standard was defocused to remain in the linear region of the CCD, and since the seeing changed quite a bit during the nights. Each standard star is isolated from any companion by more than 25 pixels. The sky values were determined locally for each standard star from a clipped average in a 25–30 pixel annulus around each star. The statistical error in each measurement was less than 1%. For most stars, it was very much smaller than 1%.

We identified three nights in the November run and two nights in the December run which were basically clear. For each run, we chose several stars observed on all nights as the basis for our calibration. In order to reduce the number of degrees of freedom we were fitting, we force the zeropoint to be the same on each night in a run. (When allowed to vary, the zeropoint shifted by 1 to 7 percent from night to night. Since we do not cover a large airmass range, we are fairly insensitive to, and little affected by, the individual values of the zeropoint and extinction; errors in determining the zeropoint are typically absorbed into the extinction term.) We then employed a least-squares algorithm to solve for the relative exoatmospheric magnitudes of the standard stars (forced to be the same at all times) and for the first-order extinction on each night (allowed to vary from one night to another). Finally, we shifted the output relative magnitudes of all stars by a constant value in order to give the fundamental standard BD +17°4708 its fiducial SDSS magnitudes.

In Table 4, we list the parameters of the photometric solution for each of the five nights we used to calibrate our data. Note that the RMS residuals from the solution for the bright standard stars range from 2% to 7%. It is likely that systematic errors of similar size appear in our photometry for the faint objects in our selected fields, since these residuals indicate the extent to which the nights were not photometric. The magnitude of each object in each filter was determined using the zeropoints and extinction values in Table 4, and is given by:

$$m = \text{zeropoint} - 2.5 \log \left(\frac{\text{counts} \times \text{aperture correction}}{\text{exposure time}} \right) - \text{extinction} \times \text{airmass}. \qquad (1)$$

One field, LBQS 2231-0015, was observed four times over three nights. Calibrating each observation separately, then comparing magnitudes from one image against those of another, we find systematic differences of less than 4% in all but a single case (one pair of u^* images has an offset of about 14%). This test measures systematic errors not just from the non-photometric nights, but also from aperture corrections. The conclusions of our work are affected slightly by these small errors, and so we attempt to correct for them in §6.

5. Catalog of u^*, g^*, r^*, i^*, z^* Photometry

Table 5 contains a catalog of 2261 astronomical objects (334 extended sources, 1915 point sources, and 12 known QSOs) from the 22 fields observed. The objects are organized by field; the fifteen deeper fields are listed first, followed by the fields containing the standard stars. Within each category, the sources are listed in order of right ascension. Each entry is identified by the the IAU acronym NRRF assigned to this catalog, plus the sequence in the format JHHMMSS.s+DDMMSS. In this section, we describe the construction of the catalog from the measured objects, and elucidate its properties through a series of plots.

There were a total of 5555 objects detected in the fifteen deep fields. Many of these objects are not astronomical, but rather they are cosmic rays, diffraction spikes, etc. Histograms of the star counts in this first catalog are shown in Figure 2. From this figure, we estimate completeness limits of $21.0, 20.5, 20.5, 19.5$, and 18.5 in u^*, g^*, r^*, i^*, and z^*, respectively.

The star-galaxy separation is pretty solid about one magnitude brighter than the completeness limit, so we conservatively limited the catalog at $r^* < 19.5$. With the magnitude cut alone, the list was cut down to 1826 sources, most of which were real.

One of the authors (H. N.) then looked at the image of each source in all five passbands, and threw out suspect measurements. Measurements were rejected if they were (a) in the tails of a bright star, (b) on a diffraction spike, (c) improperly centered (pulled off by a neighboring star), (d) within 7 pixels of a cosmic ray hit, (e) within ten pixels of a similar or brighter object, (f) in a region of the CCD affected by a reflection, (g) vignetted (this happened in several cases where the filter wheel didn't move to the correct position), (h) part of a galaxy whose center was another object, or (i) part of a galaxy which was more than 3 times wider than the aperture (there were 3 galaxies affected by this criterion). It was not too uncommon for cosmic ray hits to affect significantly the u^* measurement of objects near the detection limit. If in doubt, the measurement was tossed out. If the r^* measurement was rejected, then the object was removed from the catalog. The effect of this is that a non-detection in the catalog can either be due to the object being too dim, too bright, near another astronomical object, or near a defect in the image. Eleven percent of the objects were removed from the catalog, leaving 1630 bona fide astronomical objects. Fainter objects were removed from the catalog at a somewhat higher rate since they were more likely to be affected by neighboring objects or defects.

The resulting catalog is a census of the colors of objects in SDSS filters to a limiting magnitude of about $r^* = 19.5$. This is approximately the spectroscopic limit of the Sloan survey. More attention was paid to ensuring that the magnitudes of the table entries were correct than to ensuring that every object was measured in every filter.

Figures 3, 4, and 5 show the color-color plots for the deep sample. Somewhat more than half of the objects were detected in u^*. Those which were not detected were usually fainter or red (see Figure 4). Ninety percent were detected in g^*, i^*, and z^*. By definition all objects were detected in r^*. The galaxies, stars, and QSOs separate nicely in $g^* - r^*$ vs. $u^* - g^*$ plot. The QSOs cross the stellar locus at $z \sim 2.6$, but even there we find very few fainter stars. The sample of QSOs (Table 6) is enriched in comparison with the stars and galaxies, since thirteen of the fields were pointed at known QSOs of intermediate redshift. One of the QSOs (at $z = 2.912$) was removed from the catalog because it coincided with an artifact in that particular image. The QSO at $z = 3.408$ was not detected in the u^* image at all. Only about half of the stars and galaxies detected, primarily the blue ones, had u^* measurements.

We present the color-color plots as a function of magnitude in Figure 6. The magnitudes were divided up so as to have approximately the same number of objects in each of the $r^* - i^*$ vs. $g^* - r^*$ plots. We calculated the approximate color completeness limits assuming all stars in a given plot had the fainter magnitude limit, $r^*_{fainter}$. Thus, the completeness limits are: $(u^* - r^*) = (u^* - g^*) + (g^* - r^*) < 21.0 - r^*_{fainter}$, $(g^* - r^*) < 20.5 - r^*_{fainter}$, $(r^* - i^*) > r^*_{fainter} - 19.5$, and $(r^* - z^*) = (r^* - i^*) + (i^* - z^*) < r^*_{fainter} - 18.5$. The brightest stars are not limited by the magnitude limits. As we go fainter, the $g^* - r^*$ vs. $u^* - g^*$ plots start to lose completeness on the red end. The $g^* - r^*$ vs. $r^* - i^*$ plots start to lose completeness on the red end at about 19th magnitude in r^*. The $r^* - i^*$ vs. $i^* - z^*$ plots start to lose completeness on the blue end at about magnitude 18.5 in r^*.

The stellar locus is not as wide in the $g^* - r^*$ vs. $r^* - i^*$ plots as it is in the other two views. The width in $i^* - z^*$ is primarily due to calibration differences between fields, as is obvious from the color-color diagrams of individual fields. Figure 7 shows the color-color diagrams for each field, including the fields containing the standard stars. Catalogs for the standard star fields were generated in an identical fashion, except that the limiting magnitude was chosen to be 17 rather than 19.5 in r^*. The seven standard star fields contain a total of 631 astronomical sources.

The catalog photometry can be evaluated on three levels: (1) the relative photometry of objects in a given field, (2) the relative photometry between fields, and (3) the similarity of the system we define to the final SDSS photometric system. The errors quoted in the catalog give an estimate of the errors from photon statistics. Tests show that these are reasonable estimates of the relative photometry of objects within a field, though there are some outliers which are the result of undetected cosmic rays, holes in the flatfield, or imperfect fringe subtraction in the z^* filter. Figure 7 shows that the color-color plots within a frame are quite tight.

Relative photometry from one frame to another is affected by non-photometric conditions, imperfect aperture corrections, and errors in the determination of zeropoints and extinction coefficients. By far the most important of these is the non-photometric conditions. We can estimate the magnitude of all of these errors together by looking at relative photometry in fields which were imaged on more than one night; all of the standard star fields, and a few of the deep fields, were imaged multiple times (see, for example, Fig. 10). Measurements of the same star (or star field) on different nights typically differed by about two percent, but one in ten frames deviated by more than 5%, and one in a hundred differed by more than 10%.

The accuracy of our photometric system can be estimated by comparison with Krisciunas, Margon, and Szkody (1998) and with expected magnitudes of the standard stars as calculated from published UBVRI photometry and transformations from Fukugita et al. (1996). We have four standard stars in common with Krisciunas, Margon, and Szkody (1998). The difference in r^* for these stars is about 5%, which is somewhat higher than our quoted photometric error of about 2%. The colors are in much closer agreement, especially for redder colors. Krisciunas, Margon, and Szkody (1998) do not quote errors for their standard star measurements; if their photometric errors are similar to ours, then the colors agree within the errors. In §6 we show that for G stars our colors agree with Krisciunas, Margon, and Szkody (1998), as well as the transformations from Fukugita et al. (1996), within a few percent. This is the best one could expect considering the errors from frame to frame due to non-photometric conditions. However, colors in the systems could differ much more ($> 10\%$) for the reddest M stars.

6. Analysis

First we study the position of the locus in color space as a function of magnitude and galactic position. For this purpose we find it useful to apply a parameterization of the stellar locus similar to that described by Newberg and Yanny (1997). Using the procedures they describe, one translates the $u^* - g^*$, $g^* - r^*$, and $r^* - i^*$ positions of each star into a position along the stellar locus (k), and the positions along the major (l) and minor (m) axes of the locus cross section. This is basically a non-linear principal component decomposition.

For simpler comparison with Kurucz models, we used the locus parameters from Lenz et al. (1998). This locus was generated from synthetic photometry derived from Kurucz model stars. The locus was chosen to separate stars by temperature, surface brightness, and metallicity as well as possible; it does not follow our observed locus of stars, especially at the red end. The later part of the locus follows synthetic photometry for [Me/H] = -1.0, $\log g = 1.0$. Figures 3 and 4 indicate the center of the parameterized locus (from the Kurucz models — not our data) and approximate k values (in magnitudes) along the locus. The deviation of the observed stars from the locus fit we used may indicate that the cooler stars are higher surface gravity or lower metallicity; it does not indicate a failure of the Kurucz models, nor a problem with the calibration of our data.

Figure 8 shows the variation in l and m as a function of r^* magnitude and galactic position for stars with $2.5 < k < 3.6$. This is roughly the area of the locus occupied by stars in the temperature range $4500 < T < 6000$ (Lenz et al. 1998). According to Allen (1973), stars in this temperature range have spectral types from early G to early K. One can see a clear increase in the average value of l (the major axis length) from bright to faint stars; there is little variation in l as a function of galactic position, and little variation in m with any of the variables.

It is instructive to compare the locus position that we measure with the position we would expect from measurements of the variation in metallicity with scale height measured by Trefzger, Pel, and Gabi (1995), and the relationship between metallicity and locus position from Lenz et al. (1998). First, we must determine the absolute magnitudes of the stars in this range. From Allen (1973), a luminosity class V star with spectral type G0 has absolute magnitude $M_V \approx 4.4$ and $B - V \approx 0.58$. Interpolating his data, a main sequence early K star has $M_V \approx 6.5$ and $B - V \approx 1$. We will discuss the case of giant stars at the end. Using the relationship $r' = V - 0.49(B - V) + 0.11$ from Fukugita et al. (1996), the expected absolute magnitude range of stars with $2.5 < k < 3.6$ is $4.2 < M_{r^*} < 6.1$.

At any apparent magnitude, we can calculate the range of distances to these stars. Using the fact that our measurements span the range $15^\circ < b < 70^\circ$, we then calculate the range of scale heights above the galactic plane. Trefzger, Pel, and Gabi (1995) find that the variation of metallicity with scale height, z, is given by $[\mathrm{Me/H}] = -0.18z - 0.39$, where z is measured in kpc. We use $l = 0.25 - \frac{([\mathrm{Me/H}]+4.55)^2}{7.78^2}$ as an approximate fit to Figure 8 of Lenz et al. (1998); this is approximately correct for $-4 < [\mathrm{Me/H}] < 0$. The thicker solid lines in Figure 9 (this paper) show the expected range of l as a function of magnitude in our data; photometric errors and a range of metallicities at each scale height would tend to broaden the distribution outside these limits.

The overall shape of this distribution is not unlike the measured shape, but it falls 0.06 magnitudes smaller in l than the mass of observed stars. We attempt to list the possibilities which could cause such a discrepancy, without resolving its cause: a 0.06 magnitude error in the color calibration, an offset in the metallicity calibration of 0.5 dex, the presence of a large fraction of giant stars in the sample, inaccuracy of the model for metallicity as a function of galactic scale height, and reddening. This last possibility could contribute to the discrepancy, but it is unlikely to be the sole cause, since we would have expected a larger correlation in the l vs. galactic latitude plot if this were the case. Our estimates indicate that the difference in colors between stars on our system and on the Fukugita et al. (1996) system that was used to generate the synthetic colors is probably only half this size, though this is likely to contribute to the discrepancy. An offset of 0.5 dex in the metallicity calibration is quite possible; there is a discrepancy of this order between Gunn-Stryker spectra (Gunn and Stryker 1983) convolved with the SDSS filters and the Kurucz models in Lenz et al. (1998). Also, we used the relation somewhat outside the range of k over which it is meant to apply. Two other papers, Jønch-Sørensen (1995) and Yoss, Neese, and Hartkopf (1987), support the Trefzger, Pel, and Gabi (1995) measurement of the metallicity gradient in the thick disk, finding gradients of -0.2 dex/kpc and -0.18 dex/kpc, respectively. The absolute calibration of the metallicity gradient is not quoted in any of the three papers, but even though the metallicity dispersion in the data is large, they seem to agree to within about 0.1 dex.

We show as dashed lines in Figure 9 the expected locus of giant stars in our sample assuming that the metallicity/galactic scale height holds out to [Me/H] $= -4$ (20 kpc), at which point the metallicity is constant (this is equivalent to the assumption that the metallicity/l relationship is constant for [Me/H] < -4; we do not know the relationship between metallicity and color beyond [Me/H] $= -4$). We used $0.09 < M_{r^*} < 0.89$ for the giant stars (Allen 1973). This overly simplistic model shows that the discrepancy could be caused by giant stars in the sample - especially at bright magnitudes. However, the required fraction of giant stars in the sample, which would point to a population of stars at very great distances (20 kpc) above the galactic plane, is not consistent with previous surveys (see, for example, von Hippel 1992). More work, and preferably more photometric data, are required to sort this out.

If the variation in the stellar locus position is caused by metallicity gradients in the galaxy, then we would also expect to see a variation in the position as a function of galactic position. However, a quick calculation shows that this variation is several times smaller than the variation expected with magnitude. Consider our sensitivity to a star with a particular absolute magnitude. With our magnitude range, $14 < r^* < 19.5$, we cover a factor of 13 in distance. The range of galactic latitudes, $15^\circ < b < 70^\circ$, only gives us a factor of 4 in distance. The expected variation with galactic latitude is similar to or smaller than the systematic offsets in photometry between fields, and is additionally obscured by the magnitude range.

With the introduction of synthetic photometry from Kurucz models, we must ask whether there is a difference between the definition of the photometric system in Fukugita et al. (1996), which was used to create the synthetic photometry, and the system that we defined using the USNO telescope. To estimate the size of the color terms between these two systems, we transformed the Johnson-Cousins colors of our standard stars to SDSS colors using the transformations given in Fukugita et al. (1996), and compared them with our measured colors. A linear fit between the calculated colors and measured colors produced the following transformations:

$$u^* - g^* = -0.039 + 1.005(u' - g'),$$

$$g^* - r^* = 0.048 + 0.919(g' - r'),$$

$$r^* - i^* = 0.009 + 1.073(r' - i').$$

For typical G stars, the difference between systems is less than three percent. For the reddest M stars, however, the extrapolated color terms would lead to discrepancies larger than ten percent. Comparing our transformations with those of Krisciunas, Margon, and Szkody (1998), who took their data with the same telescope and instrument as we did, we find that the magnitudes of the color terms are similar, though the sign of the effect is not always in the same sense. We do not apply this transformation since we are unsure whether our calibrations or the Fukugita et al. (1996) transformations are more likely to be in error. If we did apply them, it would make little difference to the positions of the stars in Figure 9, and it would move the observed points farther from the Kurucz models in Figure 11.

The fact that the position of the locus is not well correlated with galactic position, coupled with the knowledge that the nights on which the data were taken were not completely photometric, suggests that it might be reasonable to offset each field so as to line them up. We are able to do this for the deep fields only; the loci in the standard star fields are much different due to different limiting magnitudes and significant reddening in some of the fields. Since the field LBQS 2231-0015 was observed four times, increasing our confidence in the photometry, we shifted all of the loci to lie on top of the average locus of stars in this field.

First, the offset in $g^* - r^*$ was obtained by comparing the average measurement of $g^* - r^*$ for all point sources with $r^* - i^* > 0.8$ in each field with the similar measurement in LBQS 2231-0015. The colors $u^* - g^*$, $r^* - i^*$, $i^* - z^*$ were calculated from the mean values of $(u^* - g^*) - \frac{k_x}{k_y}(g^* - r^*)$, $(r^* - i^*) - \frac{k_z}{k_y}(g^* - r^*)$, $(i^* - z^*) - 0.63(r^* - i^*)$ in the ranges $1.1 < (u^* - g^*) < 2.0$, $(g^* - r^*) < 1.0$, $0.1 < (r^* - i^*) < 0.4$, respectively. Here, the unit vector $\hat{k}$ along the locus is given by $k_x = 0.894$, $k_y = 0.415$, and $k_z = 0.163$. Since there were comparatively few stars involved with the $g^* - r^*$ alignment, we included all stars down to $r^* = 19.5$. To avoid completeness problems and increase the accuracy of the solution, only stars with $r^* < 18$ were included in the other three fits. The derived color offsets are presented in Table 7.

To test the accuracy of this technique, we used it to calculate the color offsets between the four measurements of field LBQS 2231-0015, and compared the results with the true color offsets, which were calculated using the same stars in each field. Figure 10 shows the results. For $u^* - g^*$, $g^* - r^*$, and $r^* - i^*$, the fits are within about one percent. The alignment in $u^* - g^*$ is a bit more problematic, since there are fewer stars, the locus is broader, and the position of the locus is a function of magnitude. However, the calculated shift is better than not shifting it at all, and in the case of similar fields is within a couple of percent.

In Figure 11 we plot the shifted data along with the Kurucz models from Figure 7 of Lenz et al. (1998). This shows the cross sections of the locus from the blue end at the top to the red end at the bottom. The subset of the data with small photometric errors is a reasonable fit to the locus of model points. Figure 12 shows the distribution of stars in three cross sections through the stellar locus. The offset of a few percent is consistent with the expected systematic errors in our data. The inferred metallicity of these stars is about [Me/H] = -1. The fainter set of stars with larger photometric errors is shifted towards lower metallicity – closer to [Me/H] = -2. Since we do not know the temperatures, metallicities, and surface gravities of the measured stars, we cannot determine how accurate the Kurucz models are, but the general agreement of the F and G star loci ($2 \lesssim k \lesssim 3.6$) is encouraging.

The locus of QSOs appears to cross the locus of stars where $2.0 < k < 2.5$. We observed three QSOs in this redshift range. The values of m for these QSOs are: $0.02, 0.14$, and 0.00. We had hoped that a with good photometry and an intrinsically thin locus of stars we might find the majority of the QSOs even in this region where they are known to coincide, but our indications are that the two dimensional nature of the stellar locus will only help us slightly. Another indication of this is given by Figure 13, which shows the distribution of stars, galaxies, and QSOs in the locus cross section. The mean positions of each type are well separated the wide axis of the cross section, though the distributions are wide. The QSOs are spread across the diagram due to the fact that the QSO locus crosses over the stellar locus. In the narrow axis, there is no separation of stars and galaxies at all, and less that a tenth of a magnitude between the means of the stellar and QSO distributions.

7. Conclusions

This paper presents the first catalog of objects measured with SDSS filters. Although the photometric system is not finalized and the nights were not photometric, the data is sufficient to ascertain the relative positions of astronomical objects in SDSS filters, at approximately the depth of the SDSS spectroscopic survey. Positions of classes of special objects, such as those measured in Krisciunas, Margon, and Szkody (1998) and Richards et al. (1997), can be compared with our stellar locus to see if one will be able to find them from SDSS colors alone. The stars measured here can be used to roughly calibrate other data taken through SDSS filters, before the final system becomes available to the public.

The original intent of taking this data was to aid in determining what parameters should be used to select QSOs by color in the SDSS. The QSOs measured here are at a redshift where they are most likely to be confused with normal stars. However, all of the QSOs observed fall outside the locus of stars. We do not know how the selection of the QSOs affected this result; we chose the brighter QSOs in each redshift range to reduce the required exposure length. Also, the QSOs were discovered in a variety of previous searches with their own selection biases.

Previous papers have shown that the locus of normal stars is a thin ribbon in color-color-color space for bright stars (Newberg and Yanny 1997) and those based on Kurucz models (Lenz et al. 1998). This paper shows that this model is consistent with the data for fainter stars; the width of the locus in the thin direction is consistent with the errors in the data. Using only the data with the smallest errors (and aided by shifts designed to reduce the systematics in photometry), the width is a few percent or less, and consistent with the photometric errors in the data. The agreement between the Kurucz models and the data is good - consistent with errors of a few percent or less in the synthetic photometry of stars. In the direction that the cross section is wider, the agreement is more difficult to test. Comparisons of the data with previous measurements galactic metallicity gradients and the metallicity calibrations from Kurucz models show the discrepancy could be as large as 6%.

We find that the stellar locus moves in the wider direction of the cross section as a function of magnitude. We show that this is expected from previous studies of the metallicity as a function of scale height. This effect has been ignored in previous searches for QSOs based on color distance from the stellar locus (Gaidos, Magnier, and Schechter 1993; Kron et al. 1991), partially because the photometric errors were too large for the effect to be noticeable. The SDSS will need to take this into account in the search algorithm, since its photometric errors are expected to be much smaller and since the survey covers a wide range of magnitudes and galactic positions. We expect that the position of the stellar locus will be primarily determined by the magnitude, since the height above the galactic plane varies only by a factor of 2 for a given magnitude over the footprint of the SDSS, while it varies by a factor of 25 over the expected magnitude range with errors smaller than 3% ($14 < r' < 21$).

The authors with to thank members of the US Naval Observatory in Flagstaff, AZ, especially Jeff Munn and Jeff Pier, for making the 1 meter telescope available. Thanks also to the those who built the SDSS software system, which was used in part to analyze the data. We thank Dawn Lenz for providing pre-publication copies of her tables. We are grateful to the anonymous referee for encouraging us to extend our analysis of the systematic errors.

Table 1. Fields Observed

Object	RA(2000)	DEC	date	airmass	$t_{exp}(u^*)$	$t_{exp}(g^*)$	$t_{exp}(r^*)$	$t_{exp}(i^*)$	$t_{exp}(z^*)$
UM 673	+01:45:14.19	-09:45:15	348	1.4	1800	300	300	300	900
[HB89] 0201+365	+02:04:55.96	+36:49:28	349	1.0	1800	300	300	300	900
[HB89] 0207-003	+02:09:49.28	-00:05:01	315	1.6	1800	300	300	300	1800
[HB89] 0216+080	+02:18:55.65	+08:17:37	317a	1.1	1800	300	300	300	900
LBQS 0256-0000	+02:59:03.91	+00:11:30	315	1.2	2700	300	300	300	2700
[HB89] 0308+190	+03:11:43.93	+19:13:48	349	1.1	1800	300	300	300	900
ASTROM C	+03:40:23.71	-00:02:35	348	1.2	1800	300	300	300	900
[HB89] 0636+680	+06:41:58.82	+67:58:27	348	1.2	1200	180	180	180	600
[HB89] 0642+449	+06:46:29.75	+44:51:11	317a	1.0	1800	300	300	300	900
[HB89] 0731+653	+07:36:23.94	+65:13:17	349	1.2	1800	300	300	300	900
ASTROM F	+08:05:42.79	-00:01:37	349	1.2	1800	300	300	300	900
[HB89] 0836+710	+08:41:19.97	+70:53:41	348	1.2	1800	300	300	300	900
[HB89] 0933+733	+09:37:50.89	+73:02:17	349	1.3	1800	300	300	300	900
[HB89] 0953+549	+09:57:12.58	+54:40:30	348	1.1	1800	600	300	300	900
LBQS 2231-0015	+22:34:06.94	+00:00:04	317b	1.4	1800	300	300	300	600
SA 92-342	+00:55:08.94	+00:43:27	315a	1.3	30	5	5	5	10
SA 94-242/251	+02:57:32.98	+00:17:32	349b	1.2	90	5	5	5	15
Hilt 404	+03:53:57.40	+53:12:58	348a	1.1	90	5	5	5	15
SA 95-149	+03:55:56.27	+00:07:48	348	1.4	60	3	3	3	5
SA 98-685	+06:52:08.85	-00:20:26	315a	1.3	60	5	5	5	10
RU 149G/D	+07:24:13.72	-00:32:03	348a	1.4	60	5	5	5	15
Feige 34	+10:39:38.85	+43:06:18	348b	1.0	30	5	5	5	15

Note. — Each field was pointed to to obtain either a standard star, a known QSO, or a star field observed in a separate astrometric survey. For each field, we record: column 1 (Object) - the target object; columns 2, 3 (RA, DEC) - the position of the field center (not necessarily the position of the target object) in J2000; column 4 (date) - the date of the observation (days since 1 January 1996), day 315 = MJD 50397, multiple observations of the same object on the same night are distinguished by letter designations; column 5 (airmass) - the mean airmass for all five filters; and columns 6-10 (t_{exp}) - the exposure times in seconds for each filter.

Table 2. Measured Stellar Widths in Observed Fields

Object	u^*		g^*		r^*		i^*		z^*	
	fwhm	apcor	fwhm	apcor	fwhm	apcor	fwhm	apcor	fwhm	apcor
UM 673	3.52	1.2108	3.24	1.1869	3.31	1.2044	3.06	1.2151	2.89	1.2487
[HB89] 0201+365	3.27	1.1693	2.81	1.2103	2.92	1.1837	2.87	1.1981	2.76	1.2293
[HB89] 0207-003	3.34	1.1603	3.35	1.1981	2.99	1.2178	2.95	1.2203	2.79	1.2543
[HB89] 0216+080	3.27	1.2046	2.99	1.2181	2.73	1.2666	2.70	1.2521	2.81	1.3249
LBQS 0256-0000	3.68	1.1590	3.05	1.2046	2.88	1.2391	2.96	1.2420	3.15	1.2079
[HB89] 0308+190	4.10	1.1429	3.73	1.1674	3.15	1.1929	3.04	1.2023	3.13	1.2425
ASTROM C	3.37	1.1505	3.23	1.1958	3.35	1.1859	3.21	1.1890	3.05	1.2800
[HB89] 0636+680	3.45	1.1966	3.01	1.2361	3.24	1.1976	2.96	1.2403	2.71	1.3295
[HB89] 0642+449	2.94	1.1989	2.77	1.2240	2.36	1.2537	2.27	1.2682	2.44	1.3225
[HB89] 0731+653	4.35	1.1552	3.75	1.1796	4.07	1.2228	3.74	1.2268	3.95	1.2721
ASTROM F	4.51	1.1286	4.17	1.1555	4.25	1.1660	3.87	1.1821	3.93	1.2682
[HB89] 0836+710	3.54	1.2071	3.22	1.2307	3.40	1.2615	3.40	1.2792	2.96	1.2350
[HB89] 0933+733	4.67	1.1388	4.25	1.2006	3.61	1.2205	3.29	1.2979	3.42	1.3050
[HB89] 0953+549	3.55	1.2272	3.20	1.2309	3.37	1.2508	3.43	1.2587	3.37	1.3137
LBQS 2231-0015	2.94	1.2068	2.99	1.1873	2.64	1.2265	2.47	1.2776	2.71	1.3194
SA 92-342	3.78	1.1625	3.10	1.2191	2.51	1.2407	3.23	1.1823	2.47	1.3240
SA 94-242/251	3.57	1.1628	3.75	1.1496	4.25	1.0980	3.06	1.2529	3.59	1.2984
Hilt 404	3.42	1.1672	2.99	1.2238	3.13	1.2472	2.83	1.2624	2.75	1.3103
SA 95-149	3.91	1.1610	3.71	1.1726	3.42	1.1793	2.56	1.2566	3.85	1.2095
SA 98-685	2.87	1.1877	2.62	1.2370	2.46	1.2472	2.91	1.2229	2.29	1.3354
RU 149G/D	4.08	1.1227	3.71	1.1455	2.89	1.2369	3.17	1.2349	2.83	1.3027
Feige 34	3.36	1.2101	3.12	1.2532	3.33	1.2034	2.35	1.4287	2.64	1.4105

Note. — For each color in each field, we record the FWHM in pixels and aperture correction.

Table 3. Standard Stars

Star	Num. obs.	u^*	g^*	r^*	i^*	z^*
SA 92-342	3	12.920±0.011	11.817±0.012	11.546±0.006	11.518±0.009	11.528±0.010
SA 94-242	10	12.981±0.028	11.777±0.014	11.651±0.018	11.682±0.020	11.732±0.013
SA 94-251	10	14.521±0.031	11.739±0.013	10.742±0.014	10.367±0.013	10.163±0.017
Hilt 404	2	12.564±0.004	11.513±0.005	10.829±0.010	10.506±0.026	10.252±0.006
SA 95-149	4	14.914±0.042	11.653±0.016	10.311±0.029	9.687±0.013	9.301±0.023
SA 98-685	3	13.335±0.009	12.087±0.030	11.786±0.011	11.728±0.008	11.696±0.005
RU 149D	5	12.050±0.040	11.391±0.040	11.574±0.033	11.801±0.037	11.921±0.038
RU 149G	5	14.332±0.016	13.133±0.033	12.750±0.030	12.663±0.019	12.640±0.012
Feige 34	3	10.421±0.046	10.960±0.020	11.443±0.036	11.797±0.050	12.044±0.038

Note. — The errors were calculated from the scatter in the measurements for each star. The systematic error is expected to be a few percent.

Table 4. Zeropoints and Extinction Values

	u^*	g^*	r^*	i^*	z^*
Nov. 8, 1996 (day 314)					
zeropoint	20.30	21.70	21.48	21.05	19.96
extinction	0.53	0.17	0.08	0.03	0.05
RMS	0.02	0.02	0.04	0.05	0.05
Nov. 9, 1996 (day 315)					
zeropoint	20.30	21.70	21.48	21.05	19.96
extinction	0.52	0.16	0.08	0.03	0.03
RMS	0.05	0.03	0.05	0.07	0.07
Nov. 11, 1996 (day 317)					
zeropoint	20.30	21.70	21.48	21.05	19.96
extinction	0.54	0.17	0.08	0.04	0.06
RMS	0.02	0.01	0.01	0.01	0.02
Dec. 12, 1996 (day 348)					
zeropoint	20.21	21.69	21.49	21.02	19.87
extinction	0.49	0.17	0.10	0.03	-0.01
RMS	0.03	0.01	0.01	0.02	0.02
Dec. 13, 1996 (day 349)					
zeropoint	20.21	21.69	21.49	21.02	19.87
extinction	0.47	0.17	0.10	0.04	0.01
RMS	0.03	0.02	0.02	0.02	0.02

Note. — RMS refers to the root mean square residuals from the solution for the bright standard stars.

Table 6. QSO Magnitudes

QSO	z	N	r^*	$u^* - g^*$	$g^* - r^*$	$r^* - i^*$	$i^* - z^*$
[HB89] 0836+710	2.172	1	16.772	0.269	0.156	0.088	0.190
[HB89] 0933+733	2.528	1	17.188	0.834	0.118	0.187	0.302
[HB89] 0953+549	2.579	1	17.414	0.617	0.092	−0.002	0.202
UM 673	2.719	1	16.521	0.596	0.181	−0.006	−0.006
[HB89] 0308+190	2.756	1	18.165	1.034	0.135	0.061	0.254
[HB89] 0207-003	2.853	1	17.107	0.956	0.168	0.130	0.091
[HB89] 0201+365	2.912	1	17.975	1.340	0.387	0.175	0.051
[HB89] 0216+080	2.996	2	18.084	1.572	0.256	−0.032	0.184
LBQS 2231-0015	3.020	4	17.350	1.484	0.312	0.104	0.114
[HB89] 0731+653	3.038	1	18.120	1.953	0.170	0.033	0.056
[HB89] 0636+680	3.178	1	16.533	2.059	0.388	0.239	0.165
LBQS 0256-0000	3.374	1	17.626	3.026	0.357	−0.037	−0.067
[HB89] 0642+449	3.408	3	18.624	>2.500	0.446	0.124	0.124

Note. — The magnitudes for LBQS 2231-0015, [HB89] 0216+080, and [HB89] 0642+449 are the averages of 4, 2, and 3 separate measurements, respectively.

Table 7. Color Offsets Between Fields

Field	$(u^* - g^*)$: offset	N	$(g^* - r^*)$: offset	N	$(r^* - i^*)$: offset	N	$(i^* - z^*)$: offset	N
UM 673	-0.010	7	-0.021	10	0.019	12	0.088	11
[HB89] 0201+365	0.018	48	0.069	14	-0.006	54	0.054	49
[HB89] 0207-003	0.243	9	-0.007	6	0.020	18	0.038	17
[HB89] 0216+080	0.006	9	-0.046	13	-0.026	13	0.017	13
LBQS 0256-0000	-0.041	12	-0.018	14	0.015	16	0.077	9
[HB89] 0308+190	-0.088	30	-0.079	9	-0.044	39	0.006	38
ASTROM C	-0.003	15	-0.008	12	-0.000	20	-0.003	20
[HB89] 0636+680	0.017	40	0.029	17	-0.013	54	0.026	49
[HB89] 0642+449	-0.038	83	-0.044	17	-0.013	93	-0.022	93
[HB89] 0731+653	0.009	39	0.030	18	-0.009	52	0.028	51
ASTROM F	-0.019	95	0.023	14	-0.004	116	-0.016	108
[HB89] 0836+710	0.009	16	-0.005	8	0.005	24	-0.041	17
[HB89] 0933+733	-0.006	16	-0.003	13	-0.071	20	0.060	22
[HB89] 0953+549	0.048	8	0.020	9	0.017	12	0.014	13
LBQS 2231-0015	0.004	10	0.004	4	-0.021	21	0.014	21

Note. — One can correct the photometry of each field by adding the offsets in this table.

REFERENCES

Allen, C. W. 1973, Astrophysical Quantities (London: The Athlone Press)

Fukugita, M., Ichikawa, T., Gunn, J. E., Doi, M., Shimasaku, K., and Schneider, D. P. 1996, AJ, 111, 1748

Gaidos, E. J., Magnier, E. A., and Schechter, P. L. 1993, PASP, 105, 1294

Gunn, J. E., and Stryker, L. L. 1983, ApJS, 52, 121

Jønch-Sørensen, H. 1995, A&A, 298, 799

Kron, R. G., Bershady, M. A., Munn, J. A., Majewski, Smetanka, J. J., S., and Koo, D. C. 1991, in ASP Conf. Proc. 21, The Space Distribution of Quasars, ed. D. Crampton (San Francisco:ASP), 32

Krisciunas, K., Margon, B., and Szkody, P. 1998, PASP, 110,1342

Lasker, B. M., Sturch, C. R., McLean, B. J., Russell, J. L., Jenkner, H., and Shara, M. M. 1990, AJ, 99, 2019

Lenz, D. D., Newberg, H. J., Rosner, R., Richards, G. T., and Stoughton, C. 1998, ApJS, 119, 121

Newberg, H. J., and Yanny, B. 1997, ApJS, 113, 89

Oke, J. B., and Gunn, J. E. 1983, ApJ, 266, 713

Olkin, C. B., Elliot, J. L., Bus, S. J., McDonald, S. W., and Dahn, C. C. 1996, PASP, 108, 202

Richards, G. T., Yanny, B., Annis, J., Newberg, H. J. M., McKay, T. A., York, D. G., and Fan, X. 1997, PASP, 109, 39

Russell, J. L., Lasker, B. M., McLean, B. J., Sturch, C. R., and Jenkner, H. 1990, AJ, 99, 2059

Sergey, G., Berman, E., Huang, C., Kent, S., Newberg, H., Nicinski, T., Petravick, D., Stoughton, C., and Lupton, R. 1996, Astronomical Data Analysis Software and Systems V, ed. G. H. Jacoby and J. Barnes, A. S. P. Conference Series, 101, 248

Trefzger, Ch. F., Pel, J. W., and Gabi, S. 1995, A&A, 304, 381

von Hippel, T. A. 1992, AJ, 104, 1765

Yoss, K. M., Neese, C. L., and Hartkopf, W. I. 1987, AJ, 94, 1600

This preprint was prepared with the AAS LaTeX macros v4.0.

Fig. 1.— Star/Galaxy Separation. a) We show the distribution of object widths for catalog objects with $18.5 < r^* < 19.5$. If the measured full width at half maximum is more than 10% larger than the typical full width in the image, then the object is presumed to be extended. b) We plot the distribution of measured widths for r^* 19.5 simulated stars in one image. Eighteen of the 755 simulated stars would have been classified as extended sources. If the same fraction of real stars are classified as galaxies, then about ten of the 214 extended sources (5%) are misclassified stars.

Fig. 2.— Number counts as a function of magnitude. We plot the number of objects per magnitude as a function of magnitude. The stars are from 15 deep frames (0.54 sq. deg.), with $16 < |b| < 69$. We include all sources (solid line) and point sources (dashed line). We adopt 21.0, 20.8, 20.5, 19.4, and 18.7 as the limiting magnitudes for u^*, g^*, r^*, i^*, and z^*, respectively. These are the magnitudes at which $\log A_m$ for all objects begins to deviate from a line. The plots indicate that fainter objects are more likely to be classified as galaxies than as stars. The star-galaxy separation in the catalog is taken from the r^* images only, where we use a limit of 19.5 (one magnitude brighter than the detection limit) to increase the accuracy of the identifications.

Fig. 3.— $u^* - g^*$ vs. $g^* - r^*$. The data is taken from the 15 deep fields only. The symbols indicate stars (dots), galaxies (squares) and QSOs (circles), which are labeled with their redshifts. None of the catalog entries from the 15 fields fall outside the limits of the plot. The entire catalog contains 1630 entries, of which 1344 are stars, 274 are galaxies, and 12 are QSOs. One additional QSO is included from Table 6. The solid line shows a parameterization of the stellar locus in $u^* - g^*$, $g^* - r^*$, and $r^* - i^*$ from Lenz et al. (1998). The filled circles are labeled with the distance along the locus (k) in magnitudes, with an arbitrary zeropoint at the blue end.

Fig. 4.— $g^* - r^*$ vs. $r^* - i^*$. The data is taken from the 15 deep fields only. The symbols indicate stars (dots), galaxies (squares) and QSOs (circles). None of the catalog entries from the 15 fields fall outside the limits of the plot. The solid line shows the center of the parameterization of the stellar locus. Note that there are many red objects (beyond then red end of the stellar locus fit) which did not appear in the $u^* - g^*$ vs. $g^* - r^*$ plot, since they were not detected in u^*.

Fig. 5.— $r^* - i^*$ vs. $i^* - z^*$. The data is taken from the 15 deep fields only. The symbols indicate stars (dots), galaxies (squares) and QSOs (circles). None of the catalog entries from the 15 fields fall outside the limits of the plot.

Fig. 6.— Color plots as a function of magnitude. The symbols indicate stars (dots) and galaxies (squares). The magnitude limits were chosen to so that the number of stars in the $g^* - r^*$ vs. $r^* - i^*$ plot for each range would be approximately equal. The dashed lines show the approximate completeness limits in each plot. These are calculated from the detection limits in Figure 2 and the fainter of the r^* limits. The thicker plot outlines indicate the portion which is nominally complete. The sources outside the detection limits could be intrinsically brighter objects, or objects which were detected below the nominal detection limit. The width of the locus increases somewhat as we go fainter, presumably due to increased photometric errors. Also, the population shifts towards redder

stars (this is particularly apparent in the $r^* - i^*$ vs. $i^* - z^*$ plot). This is because the redder stars are closer to us; the number of bluer stars has started to fall off since we are getting farther away from the galactic plane.

Fig. 7.— Color plots of individual fields. $u^* - g^*, g^* - r^*$, and $r^* - i^*$ plots are shown for each of the 22 fields. The width of the locus is much narrower, especially in $i^* - z^*$, indicating that some of the dispersion in Figure 6 is caused by differences between the fields. The stellar distributions for the standard star fields, particularly those at low galactic latitudes, are substantially different from those in the QSO fields.

Fig. 8.— Locus position as a function of magnitude and galactic position. We show that the locus shifts in the wide direction as the stars get fainter, but it does not shift appreciably in the thin direction. To reduce the scatter when looking for shifts as a function of galactic position, we used only stars with $r^* < 18$. Any variation with galactic position (within the range of the fields observed) is small compared to the variation with magnitude. We include all stars in the 15 deeper fields with $2.5 < k < 3.6$.

Fig. 9.— Models of the locus shift as a function of magnitude. We show the expected limits on l from the metallicity vs. scale height measured by Trefzger, Pel, and Gabi (1995) (thick lines), assuming all of the stars are main sequence stars. The data points are identical to those in Figure 8. The discrepancy between the data and the expected limits can be erased by shifting the colors of the data points by 0.06 magnitudes (narrow lines), or by shifting the inferred metallicities of the stars by 0.5 dex (dashed lines). We also show the expected limits on l using the same model for metallicity vs. scale height, but assuming all of the stars are giants (dash-dot-dot-dot line).

Fig. 10.— Accuracy of locus shifts. The field containing QSO LBQS 2231-0015 was imaged four times on three nights. For each pair of images, we plot the color differences between two measurements of the same stars as a function of the formal error in one of the measurements. The horizontal line shows the offset calculated by comparing the positions of the aggregate locus of stars in each frame (not each individual star).

Fig. 11.— Comparison with Kurucz models. We reproduce Figure 7 from Lenz et al. (1998), with our data superimposed in color. Each panel represents a cross section of the locus, going from the blue end of the locus (a) to the red end of the locus (f). The magenta dots are point sources which are detected in u^*, g^*, r^*, and i^*, and whose formal errors in $u^* - g^*, g^* - r^*$, and $r^* - i^*$ are smaller than 0.03 magnitudes. Point sources which are detected in all four filters, but which have larger errors, are plotted in green. Quasars are plotted as larger cyan dots. Not all QSOs fit within the plot ranges. The colors of each object have been shifted so as to align the stellar loci in each field with the average locus position of field LBQS 2231-0015.

Fig. 12.— Distribution of stars in the stellar locus cross section. The histograms show the distributions of l and m for the point sources in three regions of the stellar locus which correspond to Figure 11 (c,d,e). The narrower lines correspond to stars with smaller photometric errors (magenta

dots in Figure 11); the thicker lines correspond to relatively fainter stars (green dots in Figure 11).

Fig. 13.— Distribution of stars, galaxies, and QSOs in the stellar locus cross section. The distributions of stars, galaxies, and QSOs are shown using thin, medium, and thick lines, respectively. Only objects with $k < 3.6$ are plotted. Note that while QSOs, stars, and galaxies are somewhat separated in the major axis direction, they are not well separated in the minor axis direction, indicating that these objects are more or less on the same fundamental plane.

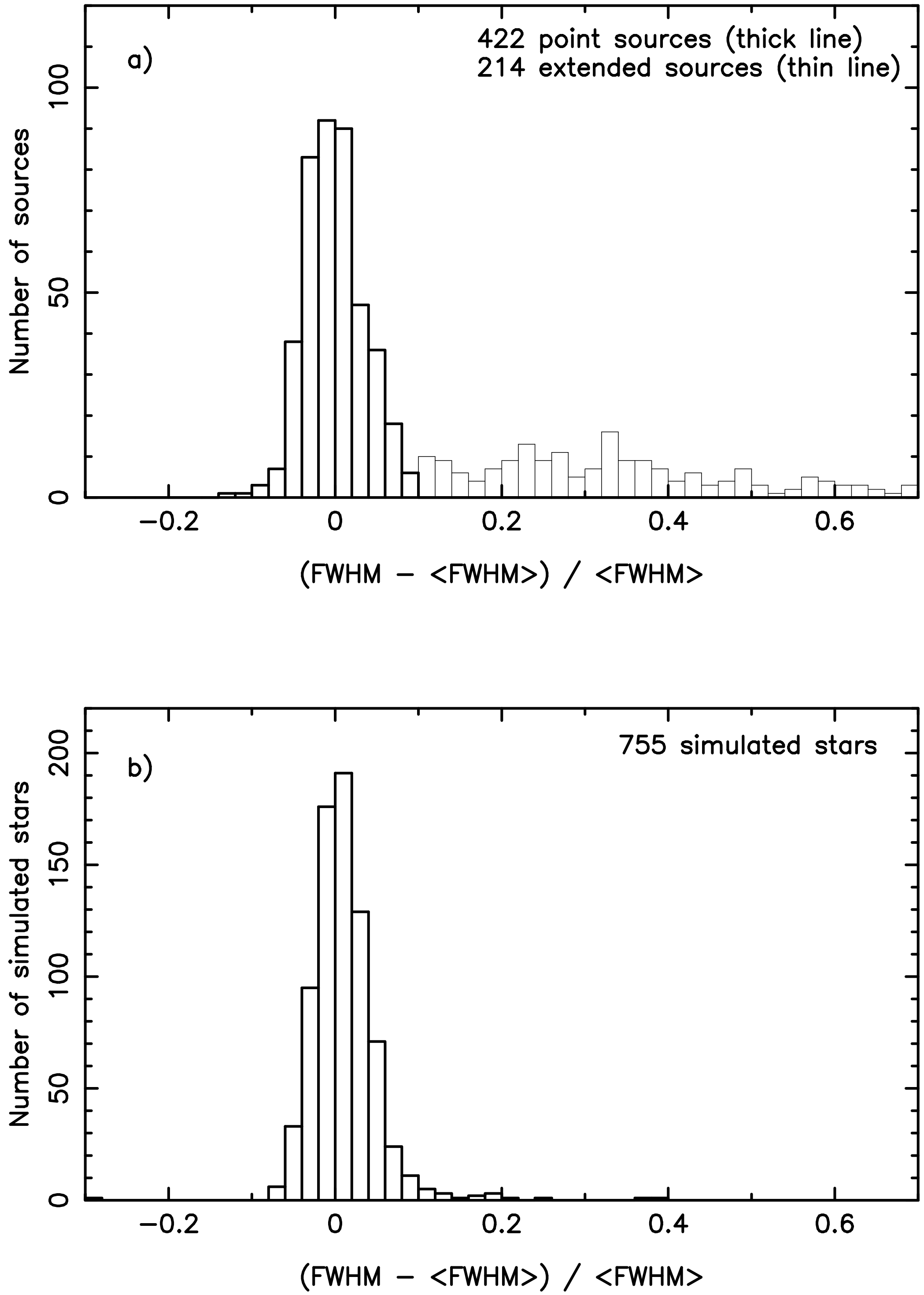
a)
422 point sources (thick line)
214 extended sources (thin line)
Number of sources
0
50
100
−0.2
0
0.2
0.4
0.6
(FWHM − <FWHM>) / <FWHM>
b)
755 simulated stars
Number of simulated stars
0
50
100
150
200
−0.2
0
0.2
0.4
0.6
(FWHM − <FWHM>) / <FWHM>

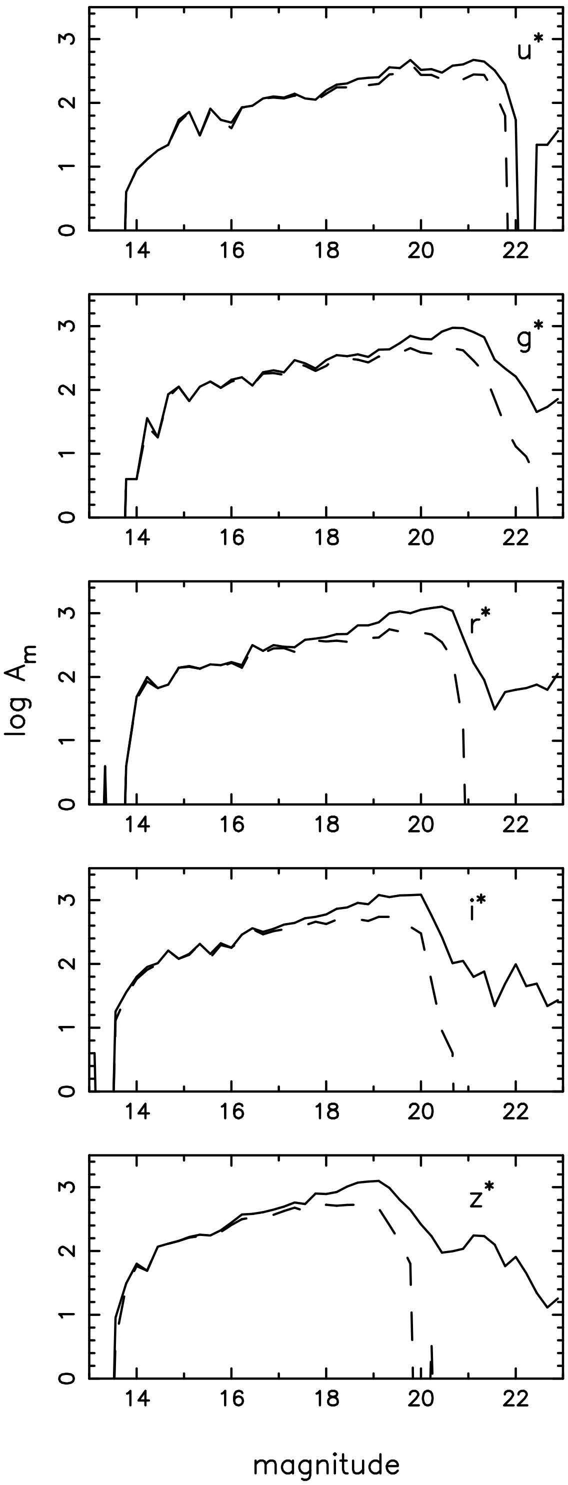
u*
g*
r*
i*
z*
log A_m
magnitude
0
1
2
3
14
16
18
20
22

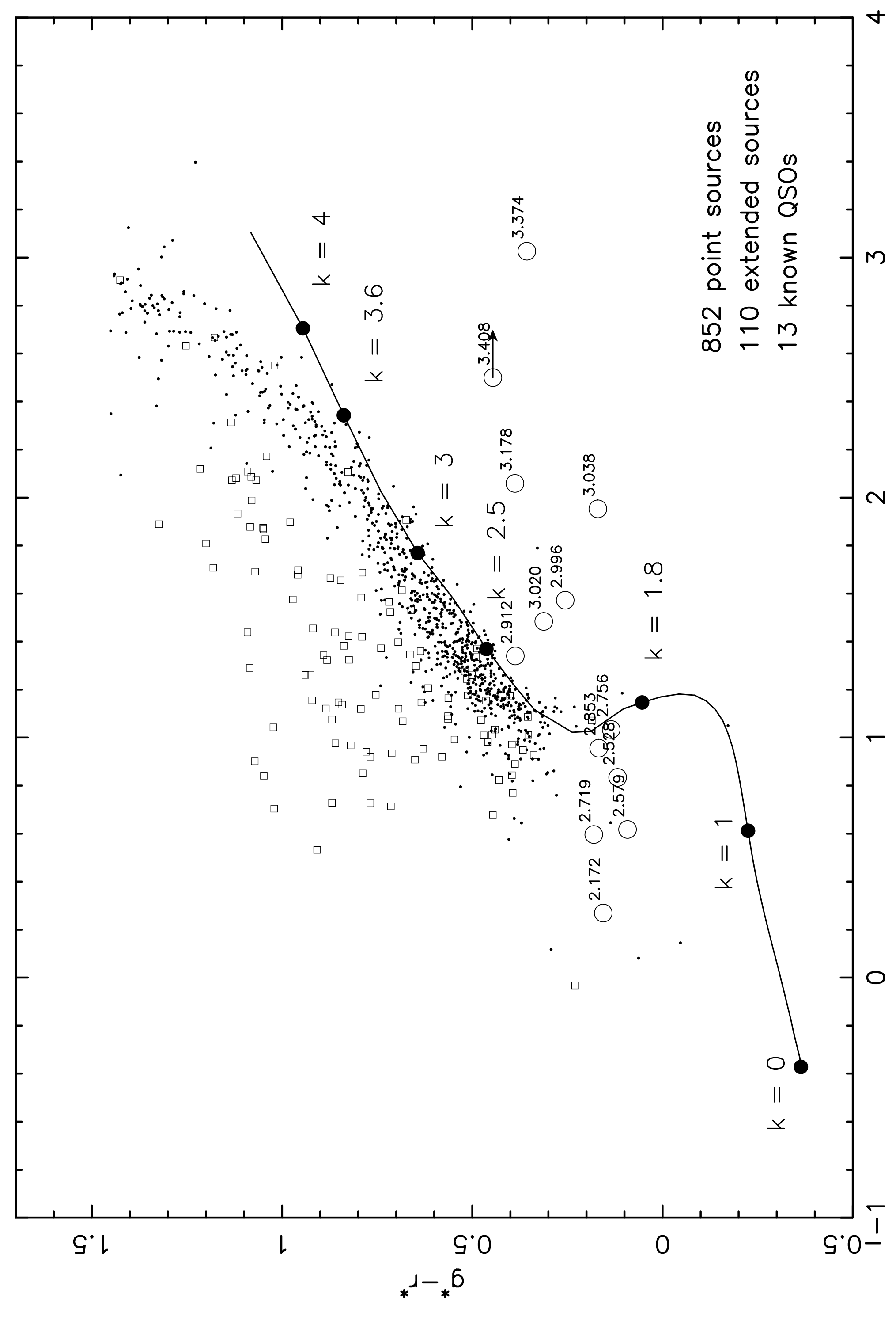
852 point sources
110 extended sources
13 known QSOs
k = 0
k = 1
k = 1.8
k = 2.5
k = 3
k = 3.6
k = 4
2.172
2.719
2.579
2.528
2.853
2.756
2.912
3.020
2.996
3.178
3.038
3.408
3.374
u*−g*
g*−r*
−1
0
1
2
3
4
−0.5
0
0.5
1
1.5

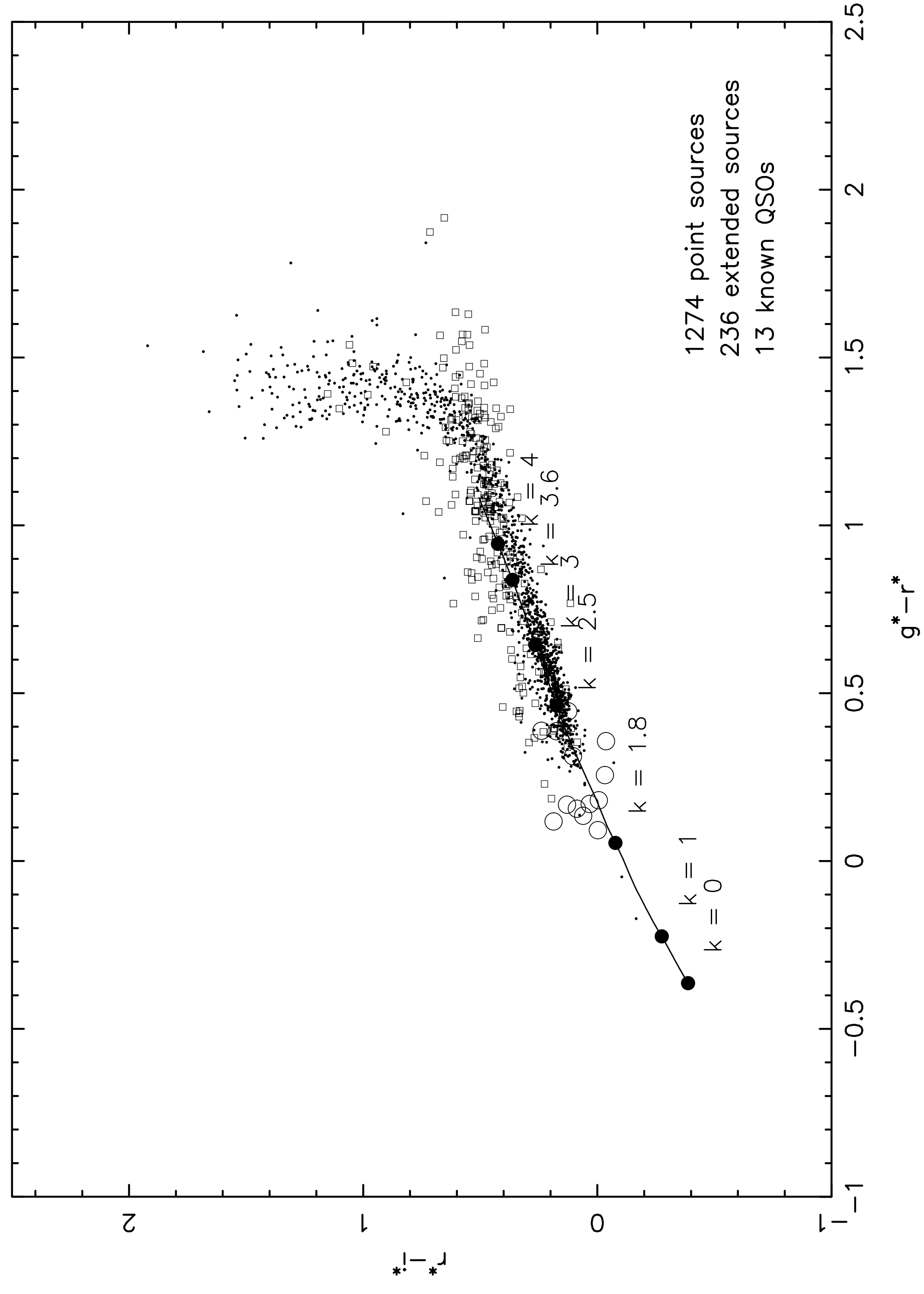
1274 point sources
236 extended sources
13 known QSOs
k = 0
k = 1
k = 1.8
k = 2.5
k = 3
k = 3.6
k = 4
g*−r*
r*−i*
−1
−0.5
0
0.5
1
1.5
2
2.5
−1
0
1
2

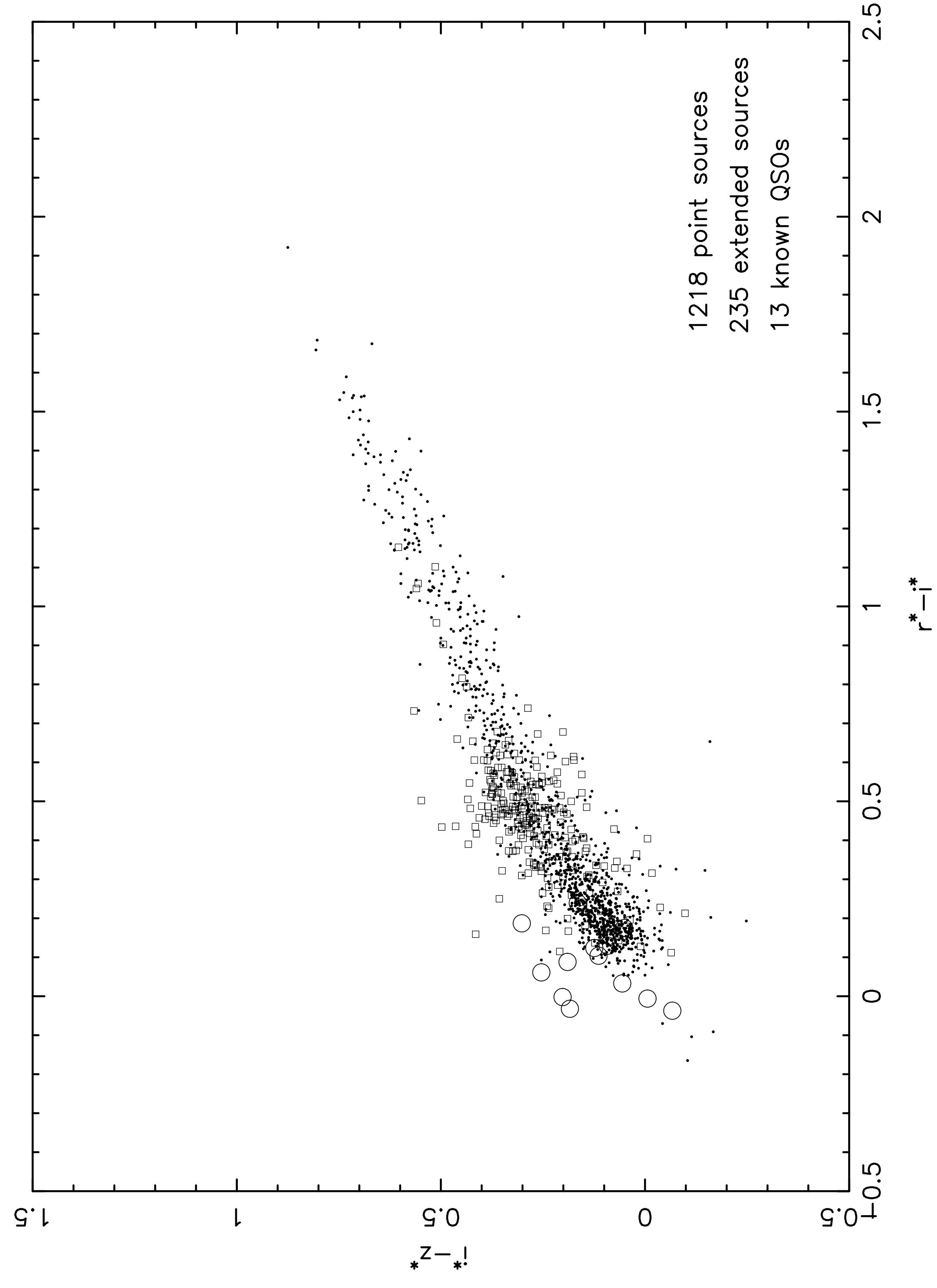
1218 point sources
235 extended sources
13 known QSOs
r*−i*
i*−z*
−0.5
0
0.5
1
1.5
2
2.5
−0.5
0
0.5
1
1.5

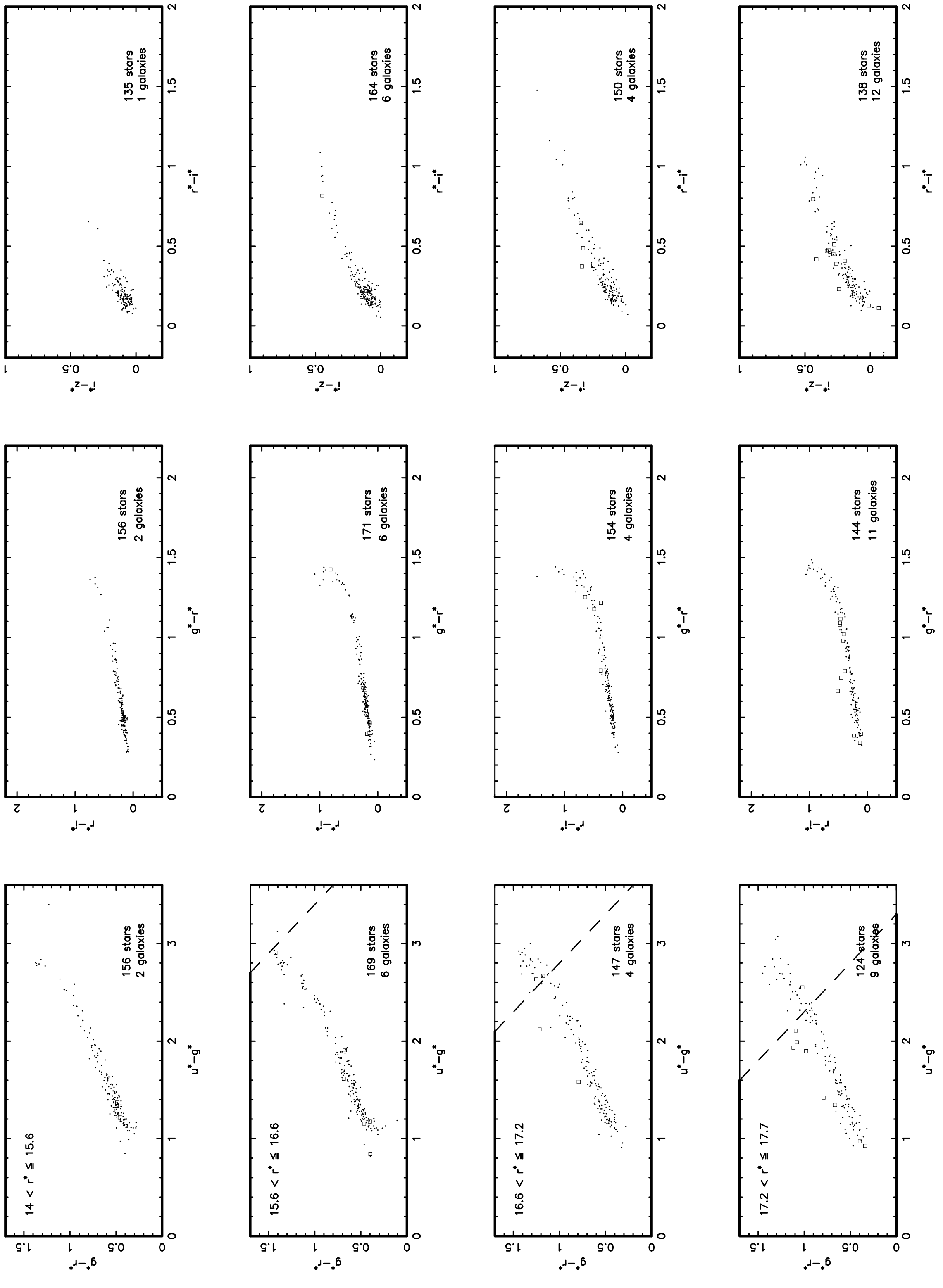
14 < r* ≤ 15.6
156 stars
2 galaxies
156 stars
2 galaxies
135 stars
1 galaxies
15.6 < r* ≤ 16.6
169 stars
6 galaxies
171 stars
6 galaxies
164 stars
6 galaxies
16.6 < r* ≤ 17.2
147 stars
4 galaxies
154 stars
4 galaxies
150 stars
4 galaxies
17.2 < r* ≤ 17.7
124 stars
9 galaxies
144 stars
11 galaxies
138 stars
12 galaxies
u*−g*
g*−r*
g*−r*
r*−i*
r*−i*
i*−z*
0
0.5
1
1.5
2
2.5
3

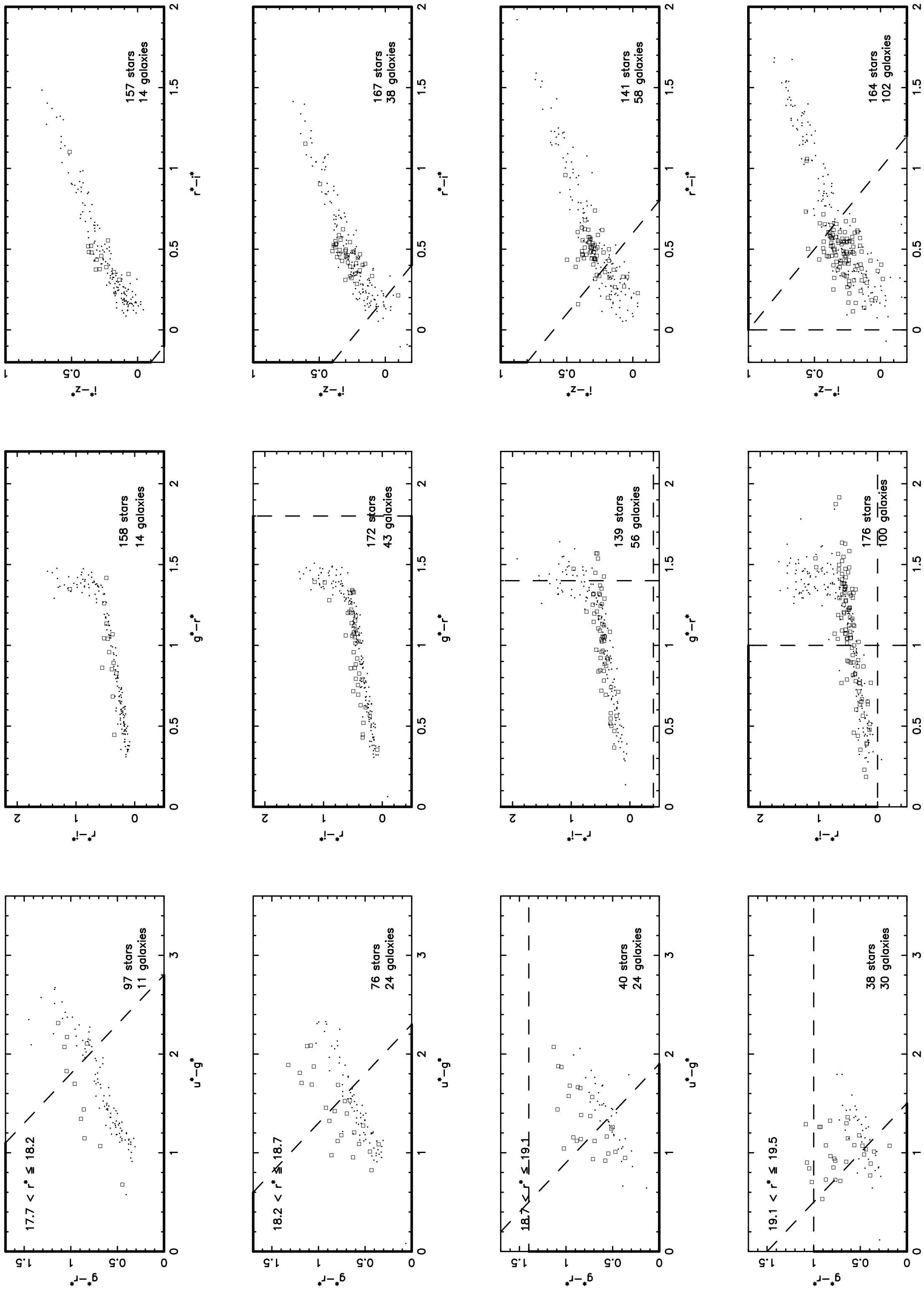
17.7 < r* ≤ 18.2
97 stars
11 galaxies
158 stars
14 galaxies
157 stars
14 galaxies
18.2 < r* ≤ 18.7
76 stars
24 galaxies
172 stars
43 galaxies
167 stars
38 galaxies
18.7 < r* ≤ 19.1
40 stars
24 galaxies
139 stars
56 galaxies
141 stars
58 galaxies
19.1 < r* ≤ 19.5
38 stars
30 galaxies
176 stars
100 galaxies
164 stars
102 galaxies
u*−g*
g*−r*
g*−r*
r*−i*
r*−i*
i*−z*
0
0.5
1
1.5
2
3

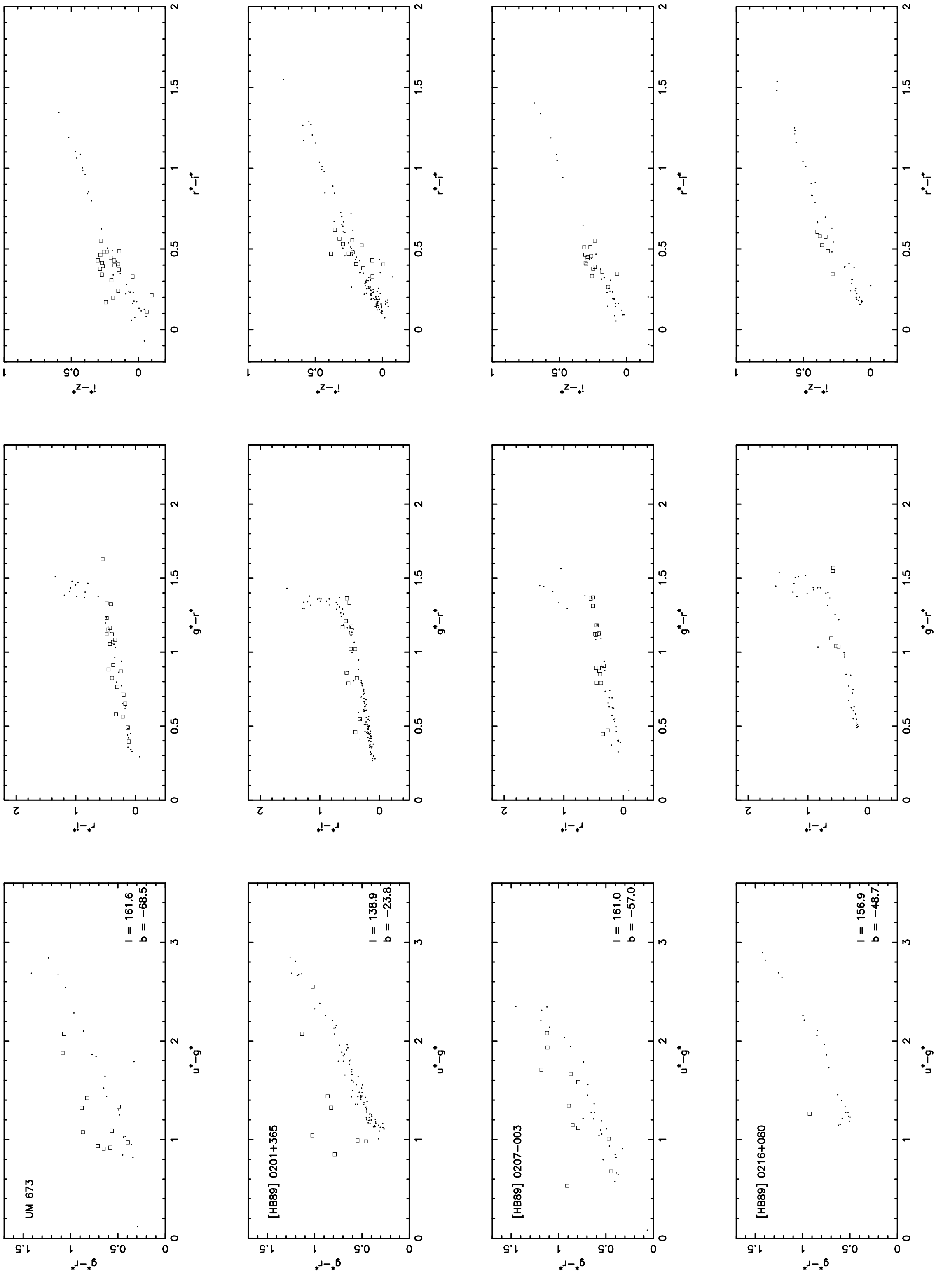
UM 673
l = 161.6
b = −68.5
[HB89] 0201+365
l = 138.9
b = −23.8
[HB89] 0207−003
l = 161.0
b = −57.0
[HB89] 0216+080
l = 156.9
b = −48.7
u*−g*
g*−r*
r*−i*
i*−z*

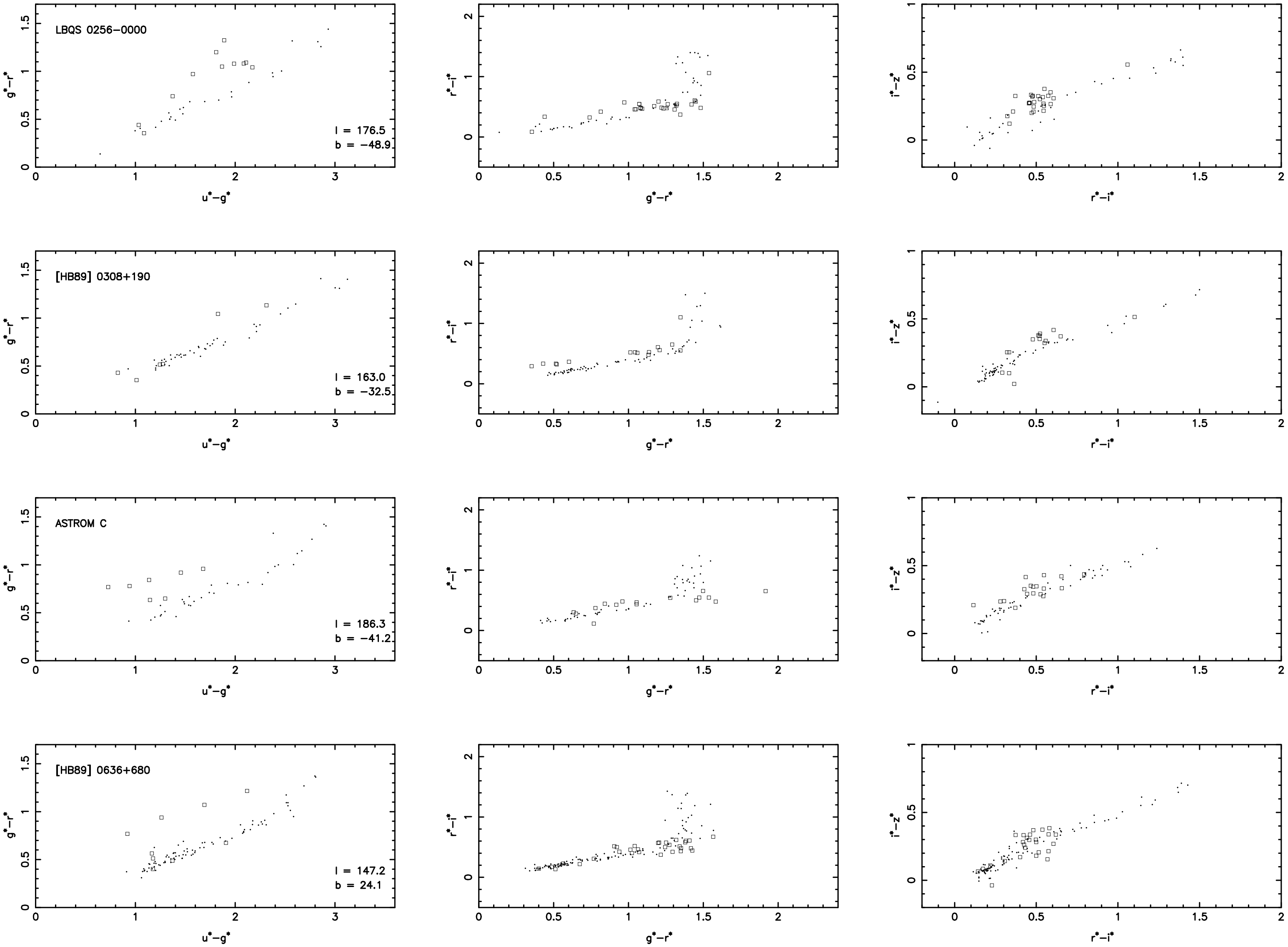
LBQS 0256−0000
l = 176.5
b = −48.9
[HB89] 0308+190
l = 163.0
b = −32.5
ASTROM C
l = 186.3
b = −41.2
[HB89] 0636+680
l = 147.2
b = 24.1
g*−r*
u*−g*
r*−i*
g*−r*
i*−z*
r*−i*
0
0.5
1
1.5
2
3

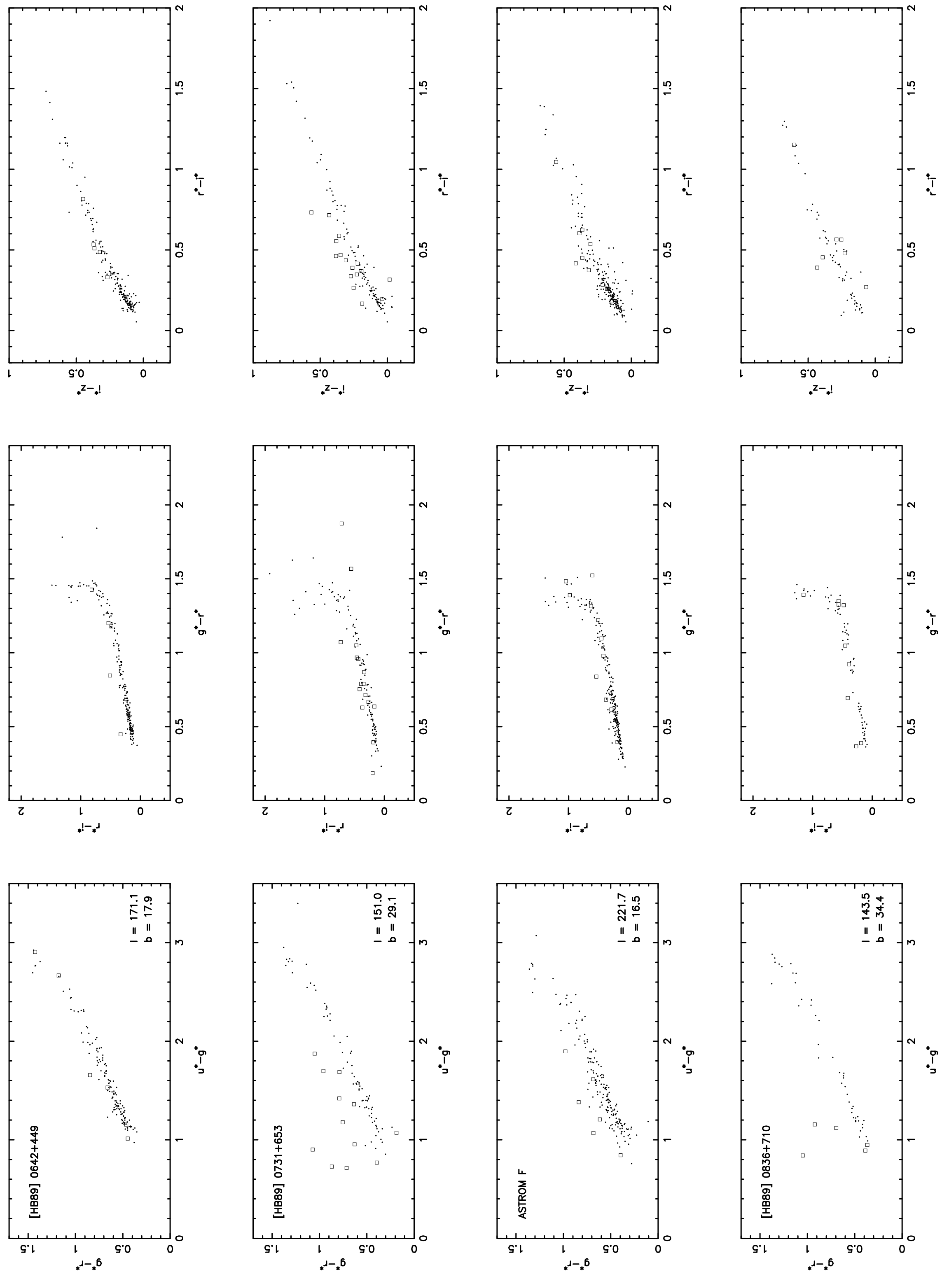
[HB89] 0642+449
l = 171.1
b = 17.9
[HB89] 0731+653
l = 151.0
b = 29.1
ASTROM F
l = 221.7
b = 16.5
[HB89] 0836+710
l = 143.5
b = 34.4
u*−g*
g*−r*
r*−i*
r*−z*
0
0.5
1
1.5
2
3

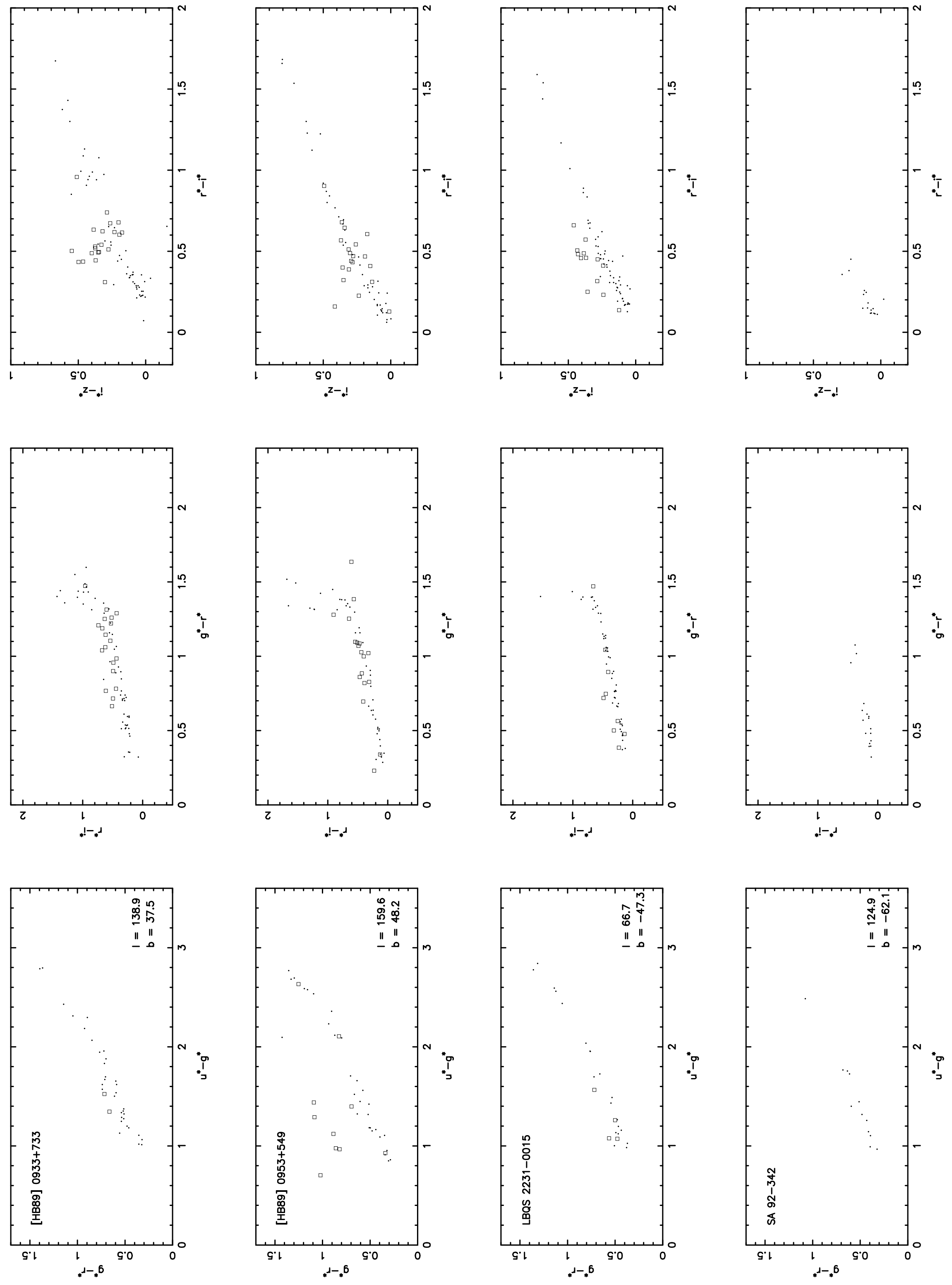
[HB89] 0933+733
l = 138.9
b = 37.5
[HB89] 0953+549
l = 159.6
b = 48.2
LBQS 2231−0015
l = 66.7
b = −47.3
SA 92−342
l = 124.9
b = −62.1
u*−g*
g*−r*
r*−i*
r*−z*
0
0.5
1
1.5
2
2.5
3

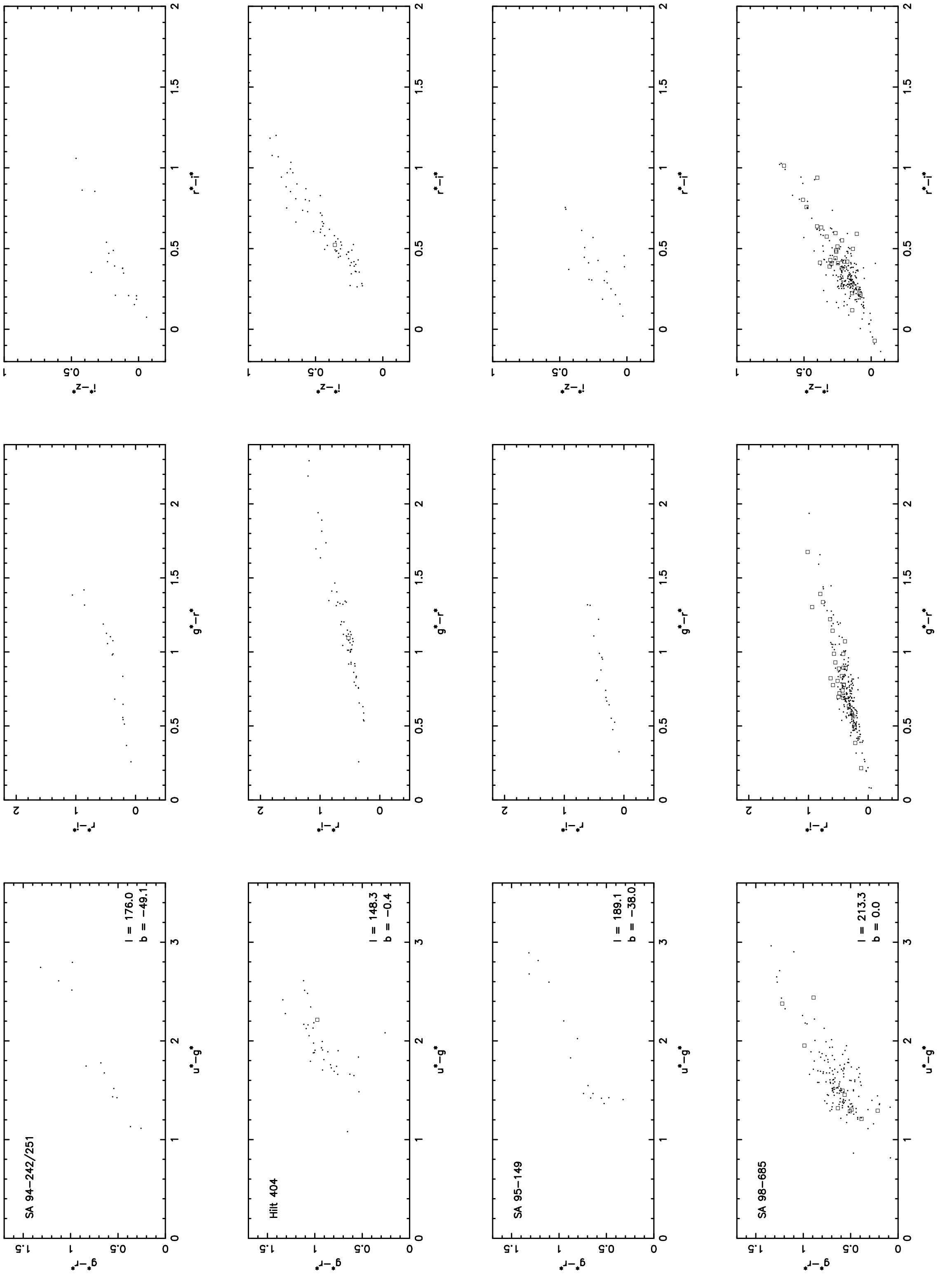
SA 94−242/251
l = 176.0
b = −49.1
Hilt 404
l = 148.3
b = −0.4
SA 95−149
l = 189.1
b = −38.0
SA 98−685
l = 213.3
b = 0.0
u*−g*
g*−r*
r*−i*
i*−z*
0
0.5
1
1.5
2
3

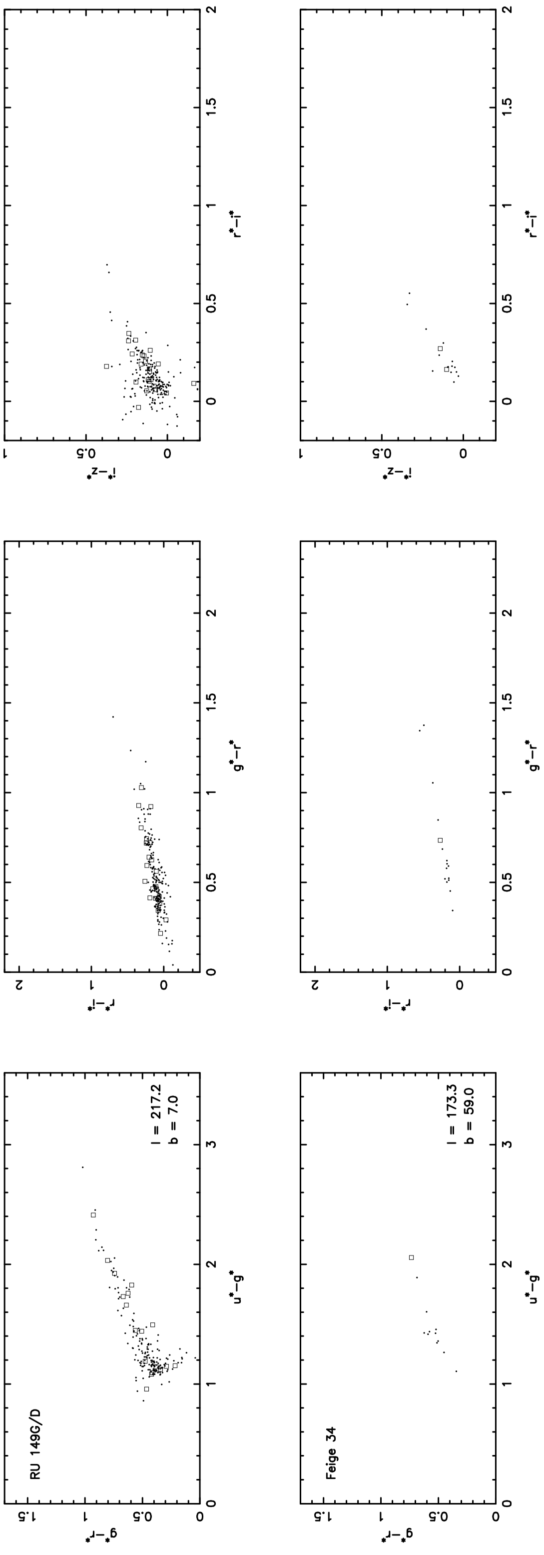
RU 149G/D
l = 217.2
b = 7.0
Feige 34
l = 173.3
b = 59.0
u*−g*
g*−r*
r*−i*
i*−z*
0
0.5
1
1.5
2
2.5
3

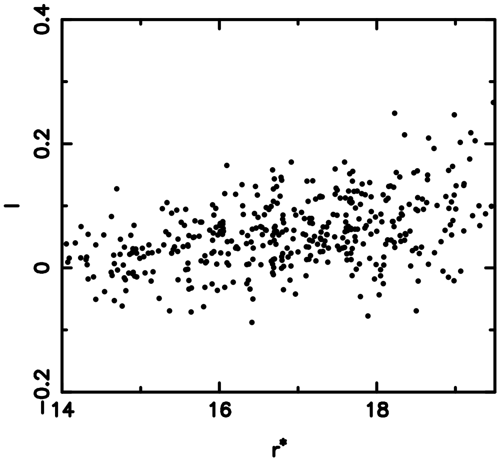
0.4
0.2
0
−0.2
l
14
16
18
r*

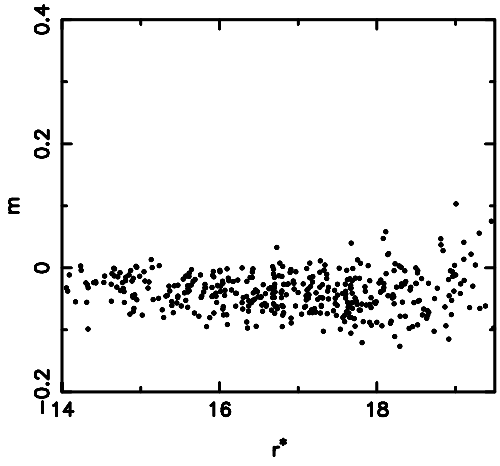
0.4
0.2
0
−0.2
m
14
16
18
r*

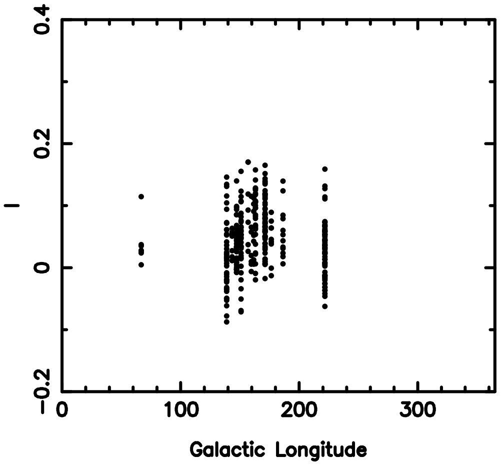
0.4
0.2
0
−0.2
l
0
100
200
300
Galactic Longitude

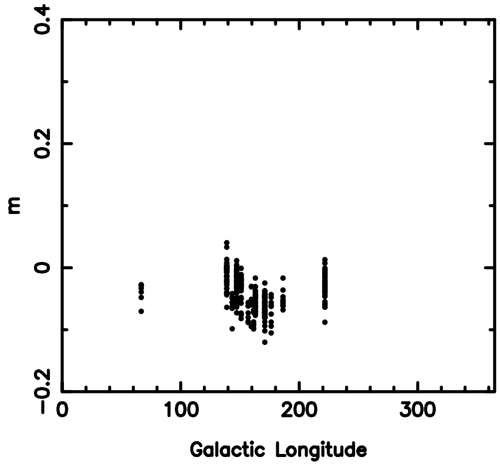
0.4
0.2
0
−0.2
m
0
100
200
300
Galactic Longitude

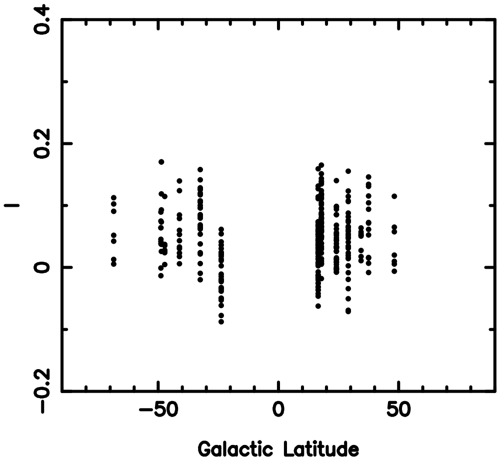
0.4
0.2
0
−0.2
l
−50
0
50
Galactic Latitude

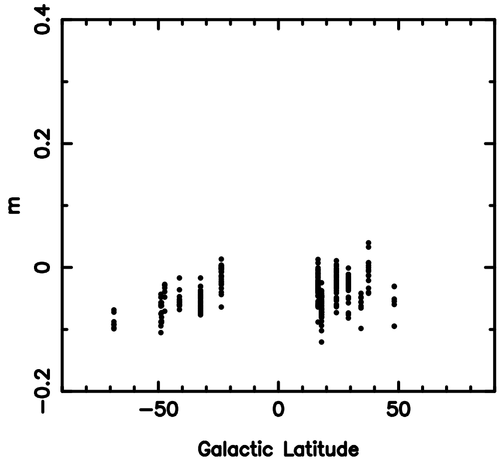
0.4
0.2
0
−0.2
m
−50
0
50
Galactic Latitude

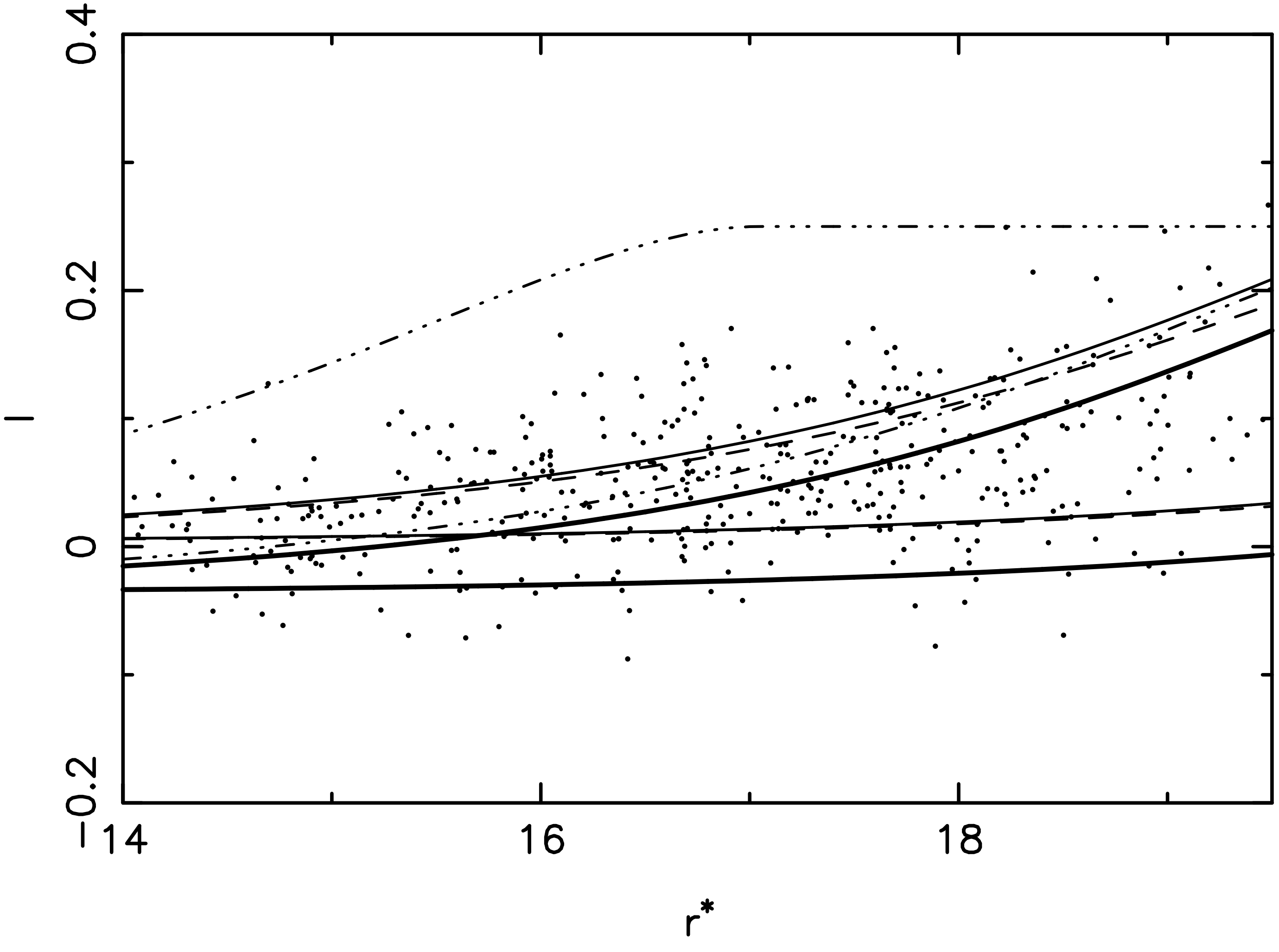
l
0.4
0.2
0
−0.2
−14
16
18
r*

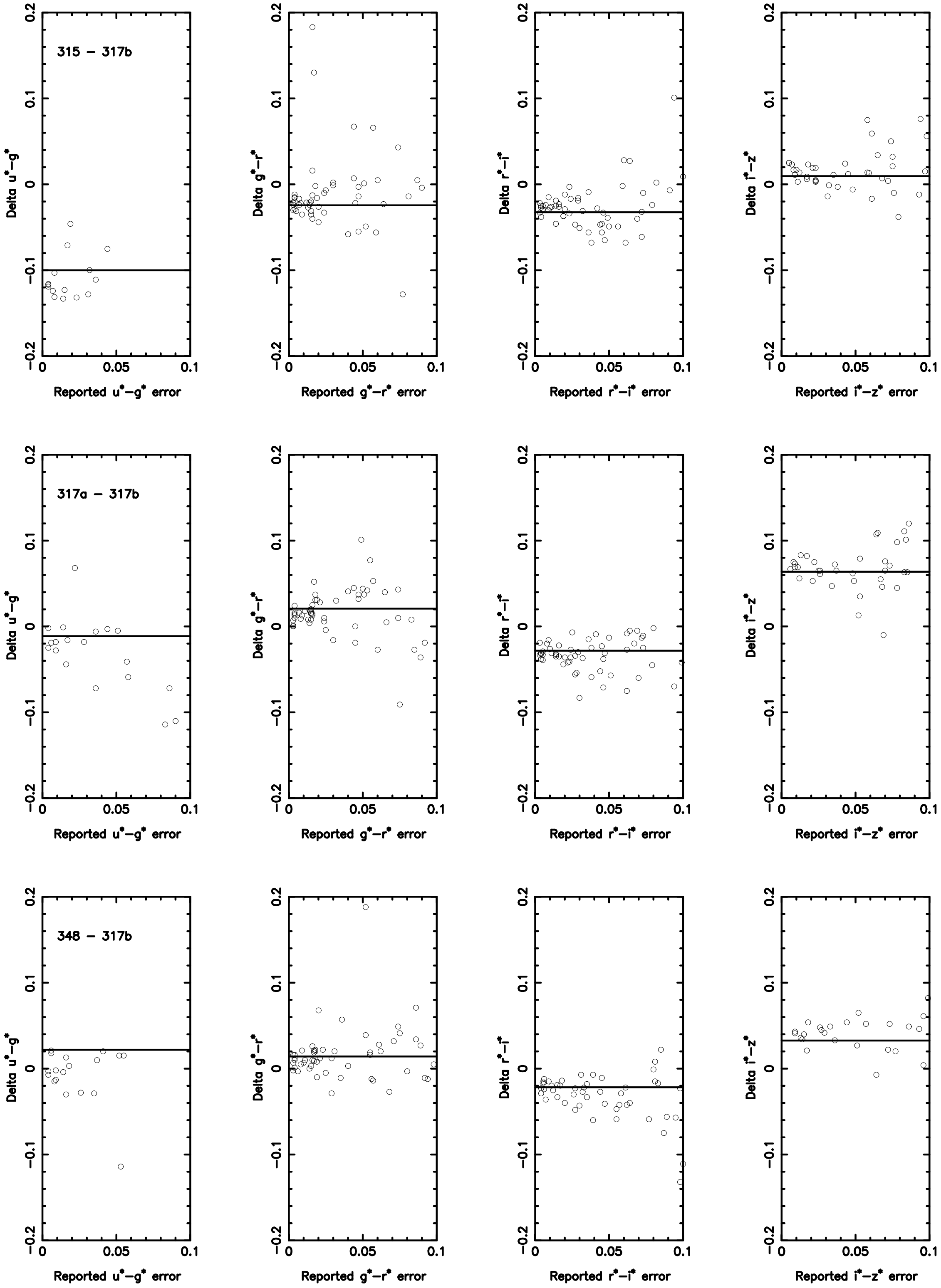
315 − 317b
317a − 317b
348 − 317b
Delta u*−g*
Delta g*−r*
Delta r*−i*
Delta i*−z*
Reported u*−g* error
Reported g*−r* error
Reported r*−i* error
Reported i*−z* error
0.2
0.1
0
−0.1
−0.2
0
0.05
0.1

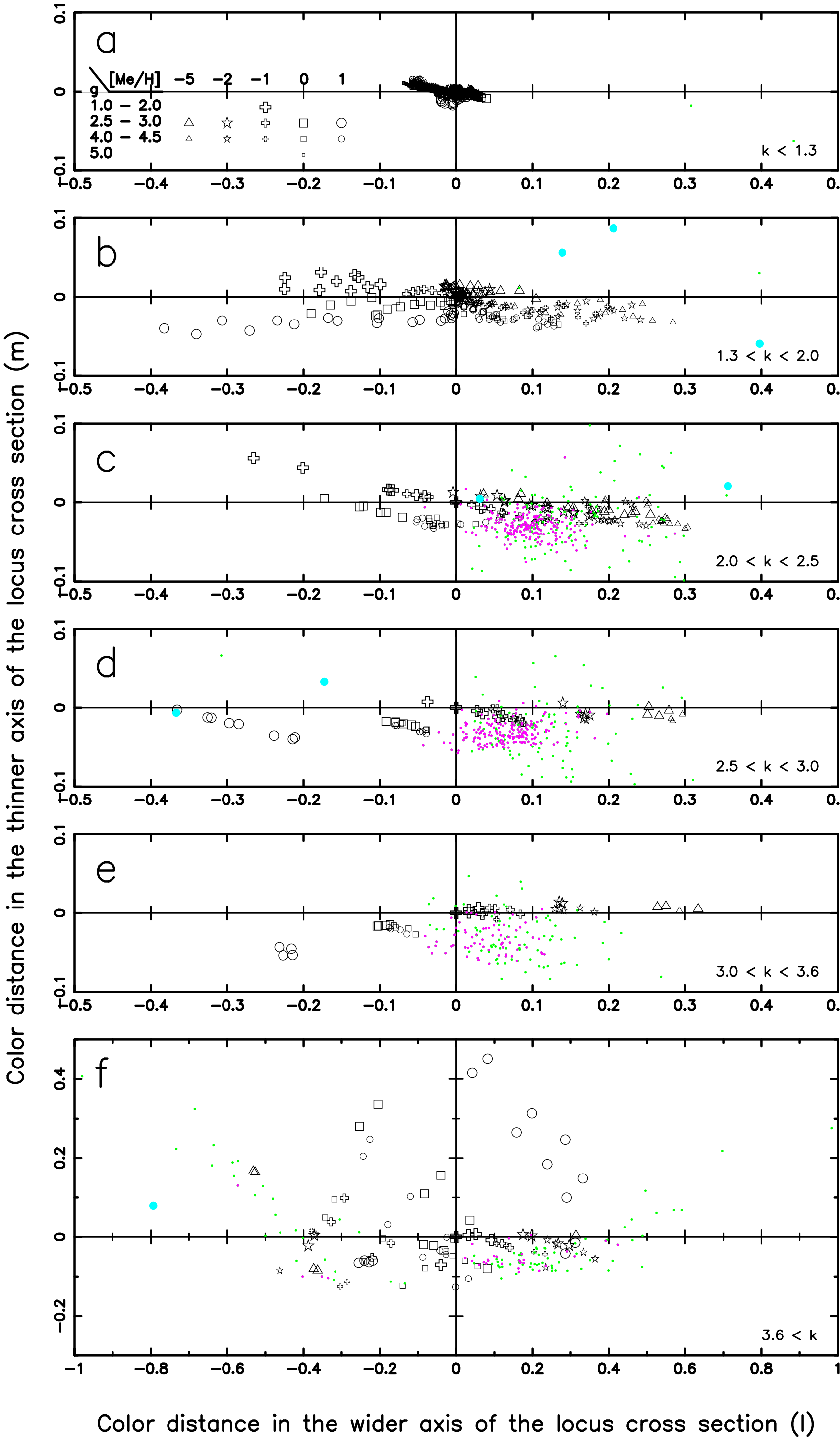
a
g
[Me/H] −5 −2 −1 0 1
1.0 − 2.0
2.5 − 3.0
4.0 − 4.5
5.0
k < 1.3
b
1.3 < k < 2.0
c
2.0 < k < 2.5
d
2.5 < k < 3.0
e
3.0 < k < 3.6
f
3.6 < k
0.1
0
−0.1
−0.5
−0.4
−0.3
−0.2
−0.1
0
0.1
0.2
0.3
0.4
0.5
0.4
0.2
0
−0.2
−1
−0.8
−0.6
−0.4
−0.2
0
0.2
0.4
0.6
0.8
1
Color distance in the thinner axis of the locus cross section (m)
Color distance in the wider axis of the locus cross section (l)

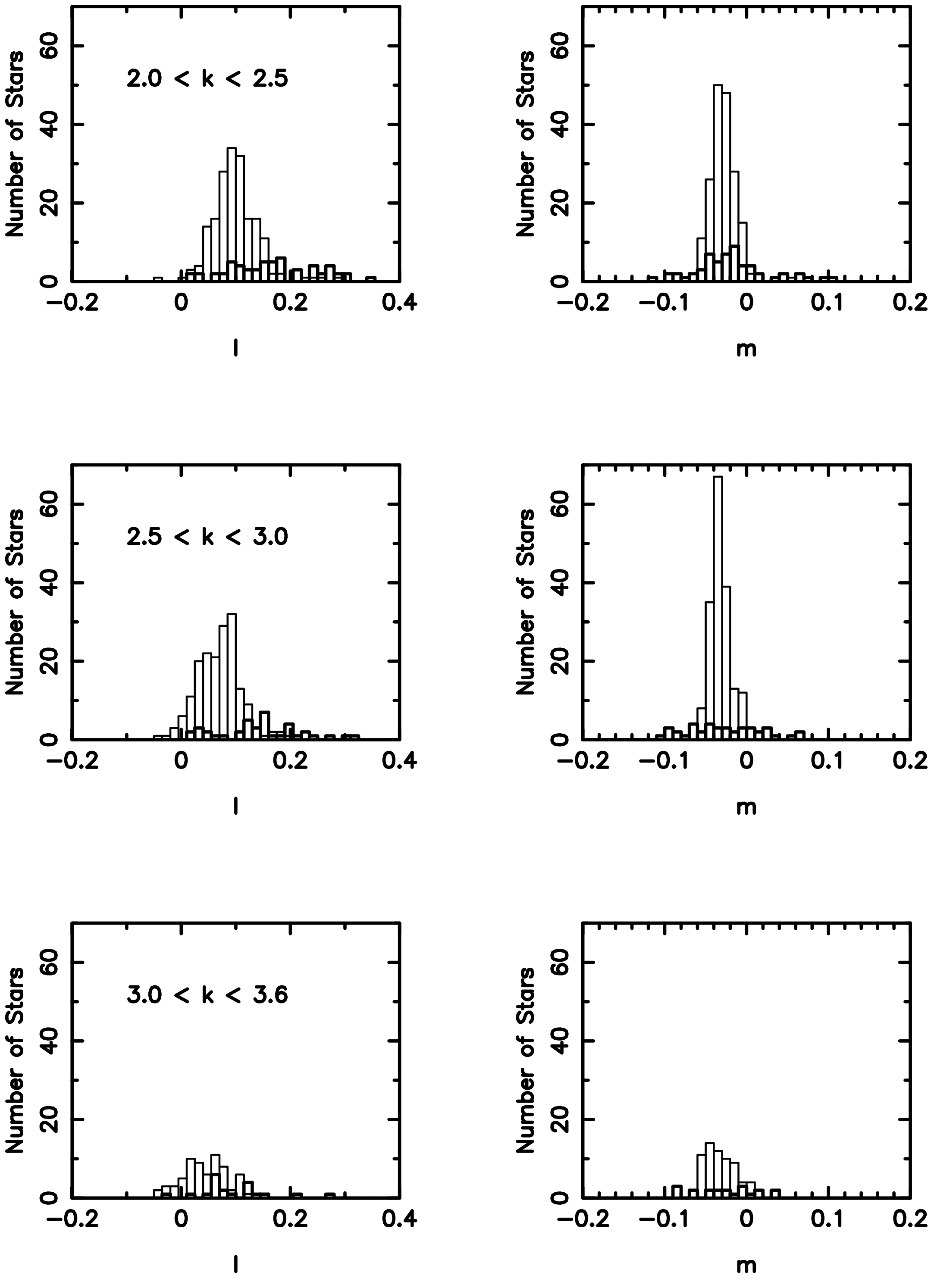
2.0 < k < 2.5
2.5 < k < 3.0
3.0 < k < 3.6
Number of Stars
0
20
40
60
−0.2
0
0.2
0.4
l
−0.2
−0.1
0
0.1
0.2
m

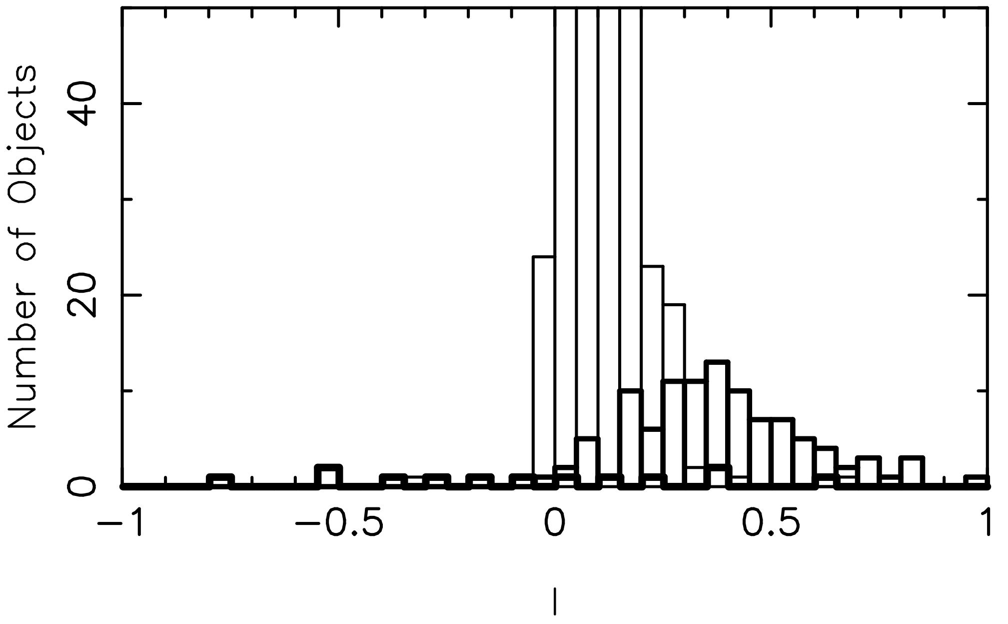
Number of Objects
0
20
40
−1
−0.5
0
0.5
1
l

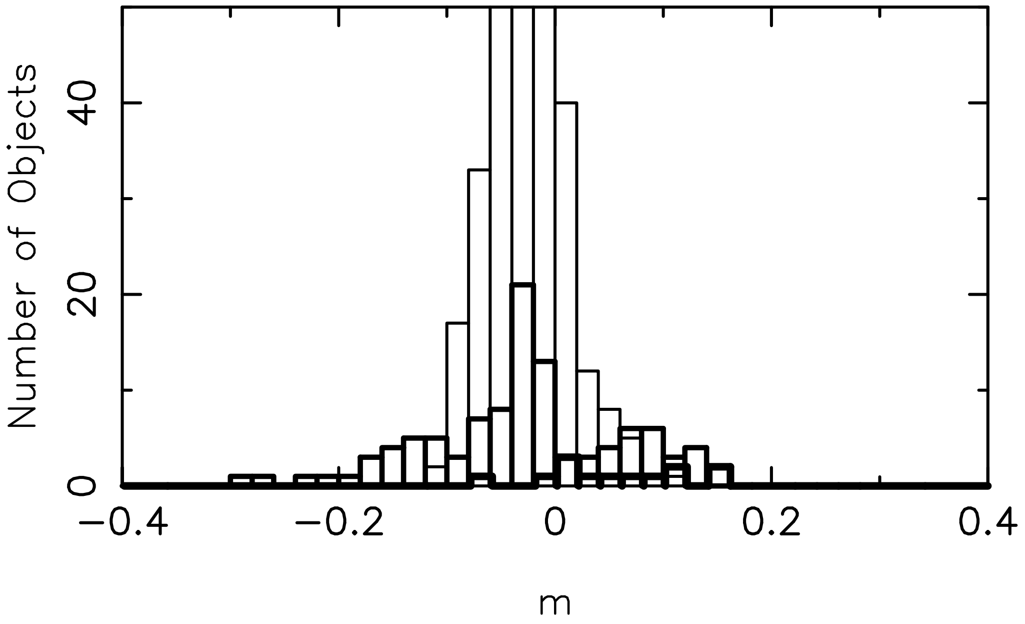
Number of Objects
0
20
40
−0.4
−0.2
0
0.2
0.4
m